

Implications of Narrow Spectra of Fast Radio Bursts

YUAN-PEI YANG^{1,2}

¹*South-Western Institute for Astronomy Research, Yunnan University, Kunming, Yunnan 650504, China*

²*Purple Mountain Observatory, Chinese Academy of Sciences, Nanjing, Jiangsu 210023, China*

ABSTRACT

Fast radio bursts (FRBs) are millisecond-duration radio transients with extremely high brightness temperatures at cosmological distances, and the physical origin and the radiation mechanism of FRBs are still unknown. The observed spectral bandwidth of some FRBs appeared narrow compared with their peak frequencies, which could be used to constrain the radiation mechanism and the astrophysical environment of FRBs. In this work, we investigate some possible physical origins of the narrow spectra from the perspectives of intrinsic radiation mechanisms, coherent processes, radiative transfers, and interference processes. We find that: (1) If the observed narrow spectra of FRBs are attributed to the intrinsic radiation mechanism by a single charged particle, the particle's deflection angle should be much smaller than the radiation beaming angle. (2) Coherent process can make cause narrow spectra. For the bunching mechanism, the narrow spectra might arise from the radiating bunches with a quasi-periodic distribution. For the maser mechanism, the negative absorption process can naturally cause a narrow spectrum. (3) Most absorption and scattering processes do not significantly change the observed spectra based on the current observation of some FRB repeaters. (4) Scintillation and plasma lensing in the FRB source environment can modulate the spectra, leading to narrow spectra and the burst-to-burst variation of spectra. A planet-like object can generate spectral modulation via gravitational lensing at the GHz band, but the observed burst-to-burst variation of the spectra does not support this scenario.

Keywords: Compact radiation sources (289); Radio transient sources (2008); Radio bursts (1339); Radiative processes (2055); Neutron stars (1108)

1. INTRODUCTION

Fast radio bursts (FRBs) are millisecond-duration radio bursts with extremely high brightness temperatures of $T_B \sim 10^{35}$ K, which suggests that their radiation mechanisms must be coherent. Some coherent emission mechanisms have been invoked to interpret the emissions of FRBs, including coherent radiation by charged bunches (Katz 2014, 2018; Kumar et al. 2017; Yang & Zhang 2018a, 2023; Lu et al. 2020; Cooper & Wijers 2021; Wang et al. 2022b; Kumar et al. 2022; Qu et al. 2023), maser by hydrodynamic instabilities or kinetic instabilities (Lyubarsky 2021; Beloborodov 2017; Waxman 2017; Metzger et al. 2019), coherent plasma radiation (Yang & Zhang 2021; Mahlmann et al. 2022), etc. However, there is no smoking gun to identify the radiation

mechanism of FRBs so far. In addition to the radiation mechanism, the physical origin of FRBs also remains an unsolved puzzle due to the diversity of FRBs (see the recent review of Zhang 2022b). FRB 200428 was detected to be associated with a Galactic magnetar SGR J1935+2154 (Bochenek et al. 2020; CHIME/FRB Collaboration et al. 2020; Mereghetti et al. 2020; Li et al. 2021; Ridnaia et al. 2021; Tavani et al. 2021), implying that at least some FRBs originate from the magnetars born from the core collapses of massive stars. However, the association between FRB 20200120E and its host globular cluster with an extremely old age challenges the core-collapse magnetar formation (Bhardwaj et al. 2021; Kirsten et al. 2022), which means that it is more likely produced by an old object or a system associated with a compact binary merger (Wang et al. 2016; Zhang 2020; Kremer et al. 2021; Lu et al. 2022).

Up to the present, hundreds of FRB sources have been detected, and dozens of them show repeating behaviors (e.g., CHIME/FRB Collaboration et al. 2021).

The increasing number of detected FRBs starts to shed light on the diversity among the phenomena, and the properties of the observed spectra provide important information about the radiation mechanism of FRBs. The first CHIME/FRB catalog identified four observed archetypes of burst morphology (Pleunis et al. 2021), including simple broadband, simple narrow band, temporally complex, and downward drifting. Meanwhile, the bursts from FRB repeaters have a larger pulse duration, narrower bandwidth, and lower brightness temperature than those of the one-off FRBs, which might be due to a beaming, propagation effect, or intrinsic populations. Law et al. (2017) made the first simultaneous detection of FRB 20121102A using multiple telescopes and found that its burst spectra could not be well modeled by a power law and more like a Gaussian shape characterized by a ~ 500 MHz envelope. Zhou et al. (2022) recently reported over 600 bursts from the repeating FRB 20201124A during an active episode and found that the sub-bursts of FRB 20201124A show narrow spectra with a center frequency of 1.09 GHz and a characteristic bandwidth of ~ 277 MHz. FRB 20220912A also has many bursts with narrow spectral bandwidth (Zhang et al. 2023). For the bursts with their spectra within the L band of the Five-hundred-meter Aperture Spherical radio Telescope (FAST), the relative spectral bandwidth of the radio bursts was found to be distributed near $\Delta\nu/\nu_0 \sim (0.1 - 0.2)$. Some FRBs show more extremely narrow bandwidth. One burst of FRB 20190711A has a central frequency of 1.4 GHz and a full-width-at-half-maximum (FWHM) bandwidth of just 65 MHz, and no evidence of any emission in the remaining part of the 3.3 GHz band of the Ultra-wideband Low (UWL) receiver system of the Parkes radio telescope (Kumar et al. 2021), which means that the relative spectral bandwidth is only $\Delta\nu/\nu_0 \sim 0.05$.

In this work, we will discuss the possible physical origins of the observed narrow spectra of FRBs from the perspectives of intrinsic radiation mechanisms, coherent processes, radiative transfers, and interference processes. The paper is organized as follows. In Section 2, we discuss the spectral bandwidth distribution and the possible physical processes affecting the FRB spectra. In Section 3, we generally analyze the radiation features of the intrinsic radiation mechanisms by a single charged particle, including the radiation mechanisms with the particle's deflection angle larger than the radiation beaming angle in Section 3.1 and the opposite scenario in Section 3.2, and the possible astrophysical scenarios are discussed in the Section 3.3. In Section 4, we discuss how the coherent processes change the radiation spectra, including the bunching mechanism in Sec-

tion 4.1 and the maser mechanism in Section 4.2. The radiative transfers (including absorption and scattering processes) are discussed in Section 5, and some interference processes (scintillation, gravitational lensing, and plasma lensing) at a large-scale region are discussed in Section 6. The results are summarized and discussed in Section 7. The convention $Q_x = Q/10^x$ is adopted in cgs units unless otherwise specified. Some detailed calculations are presented in the Appendices.

2. NARROW SPECTRA OF FRBS: OBSERVATION AND PHYSICAL ORIGIN

2.1. Spectral bandwidth distribution of FRB repeaters

Some FRBs, e.g., FRB 20190711A, FRB 20201124A, and FRB 20220912A, appear extremely narrow spectra in the bandwidths of telescopes (e.g., Kumar et al. 2021; Zhou et al. 2022; Zhang et al. 2023), implying that the spectra of at least some FRBs are intrinsically narrow. In this section, we will discuss the implication of the observed narrow bandwidths of FRBs, and emphasize that the observed relative spectral bandwidth mainly depends on the intrinsic spectral shape, the bandwidth definition (e.g., full width at half maximum, full width at tenth maximum, etc.), and the telescope's bandwidth. We first consider that the intrinsic spectra of radio bursts from an FRB source have a general form described by a broken power-law distribution,

$$F_\nu = F_{\nu,0} \begin{cases} \left(\frac{\nu}{\nu_0}\right)^{\alpha_l}, & \text{for } \nu \leq \nu_0, \\ \left(\frac{\nu}{\nu_0}\right)^{-\alpha_h}, & \text{for } \nu > \nu_0, \end{cases} \quad (1)$$

where $F_{\nu,0}$ corresponds to the maximum flux at the peak frequency ν_0 . We should notice that $\alpha_l > 0$ and $\alpha_h > 0$ are assumed here, considering that the flux F_ν vanishes at $\nu \rightarrow 0$ or ∞ . In literature, one usually defines the spectral bandwidth via the full width at a fraction of maximum ($F_{\nu,0}/N_{\text{FW}}$), e.g., the full width at half maximum (FWHM) with $N_{\text{FW}} = 2$ (e.g., Kumar et al. 2021; Zhang et al. 2023) or via the full width at tenth maximum (FWTM) with $N_{\text{FW}} = 10$ (e.g., Pleunis et al. 2021). Thus, the relative spectral bandwidth of a radio burst is

$$\frac{\Delta\nu}{\nu_0} \simeq N_{\text{FW}}^{\frac{1}{\alpha_h}} - N_{\text{FW}}^{-\frac{1}{\alpha_l}}. \quad (2)$$

We can see that the relative spectral bandwidth $\Delta\nu/\nu_0$ depends on the factor of N_{FW} and the intrinsic spectral shape that is described by the above two power-law indexes. *Since such a defined (FWHM or FWTM) relative spectral bandwidth only depends on the intrinsic spectral*

Table 1. Summary of the low-frequency spectral index α_l for various radiation mechanisms

Radiation mechanisms	Low-frequency spectral index α_l	References
Curvature radiation by a single charged particle	2/3	Jackson (1998); Yang & Zhang (2018a)
Curvature radiation by a bunch-cavity (or electron-positron) pair	8/3	Yang et al. (2020); Yang & Zhang (2023)
Curvature radiation by fluctuating bunches	0	Yang & Zhang (2023)
Synchrotron radiation by particles with a random pitch-angle distribution	1/3	Jackson (1998); Rybicki & Lightman (1986)
Synchrotron radiation by particles with a narrow pitch-angle distribution	2/3	Yang & Zhang (2018b)
Synchrotron self-absorption	5/2	Rybicki & Lightman (1986)
Jitter radiation	1	Medvedev (2000); Dermer & Menon (2009)
Blackbody radiation	2	Rybicki & Lightman (1986)
Bremsstrahlung radiation	0	Rybicki & Lightman (1986)
Inverse Compton scattering	Depend on incident photon spectrum	Rybicki & Lightman (1986); Zhang (2022a)

shape, the $\Delta\nu/\nu_0$ distribution of an FRB repeater should be narrow if the intrinsic spectral shape keeps unchanged.

Most radiation mechanisms involved in various astrophysical scenarios have a low-frequency spectral index of $\alpha_l < 3$, see Table 1. For example, the synchrotron self-absorption has a low-frequency spectral index of $\alpha = 5/2$ (Rybicki & Lightman 1986) and the curvature radiation by a bunch-cavity (or electron-positron) pair has a low-frequency spectral index of $\alpha = 8/3$ (Yang et al. 2020; Yang & Zhang 2023). Thus, for these radiation mechanisms with $\alpha_l < 3$, according to Eq.(2), the relative spectral bandwidth for FWHM with $N_{\text{FW}} = 2$ should satisfy

$$\frac{\Delta\nu}{\nu_0} > 0.2. \quad (3)$$

For example, we assume that the intrinsic spectrum is due to the curvature radiation, then one approximately has $\alpha_l \simeq 2/3$ and $\alpha_h \rightarrow \infty$ (Yang & Zhang 2018a, 2023). According to Eq.(2), the relative spectral bandwidth for FWHM is $\Delta\nu/\nu_0 \simeq 0.65$. In particular, for FRB 20190711A with an extremely narrow FWHM spectral bandwidth of $\Delta\nu/\nu_0 \sim 0.05$ (Kumar et al. 2021), one has $\min(\alpha_l, \alpha_h) \gtrsim 14$, implying an extremely narrow intrinsic spectrum that should involve some special mechanisms (that might be attributed intrinsic radiation mechanisms, coherent processes, radiative transfers, or interference processes), see the following discussions.

In reality, the bandwidth $\Delta\nu_t$ of a radio telescope is usually narrow compared with the telescope's central frequency $\nu_{0,t}$, $\Delta\nu_t \ll \nu_{0,t}$. For example, the L band of FAST is from 1 GHz to 1.5 GHz, i.e., $\nu_{0,t} = 1.25$ GHz and $\Delta\nu_t = 0.5$ GHz. Due to the limited telescope's bandwidth, many observed spectra of FRBs are often incomplete. If a radio burst is observable for a certain telescope, its emission must be within the telescope's

bandwidth, leading to the following conditions:

$$\nu_0 + \frac{\Delta\nu}{2} > \nu_{0,t} - \frac{\Delta\nu_t}{2} \quad \text{and} \quad \nu_0 - \frac{\Delta\nu}{2} < \nu_{0,t} + \frac{\Delta\nu_t}{2}. \quad (4)$$

The observed central frequency $\nu_{0,\text{obs}}$ (not the intrinsic peak frequency) of an observable FRB is in the telescope's bandwidth,

$$\nu_{0,\text{obs}} \in \left[\nu_{0,t} - \frac{\Delta\nu_t}{2}, \nu_{0,t} + \frac{\Delta\nu_t}{2} \right], \quad (5)$$

although the intrinsic peak frequency ν_0 might be estimated outside the telescope's bandwidth based on the observed spectral shape. The observed spectral bandwidth of an observable FRB is

$$\Delta\nu_{\text{obs}} = \min \left(\nu_0 + \frac{\Delta\nu}{2}, \nu_{0,t} + \frac{\Delta\nu_t}{2} \right) - \max \left(\nu_0 - \frac{\Delta\nu}{2}, \nu_{0,t} - \frac{\Delta\nu_t}{2} \right). \quad (6)$$

Since the bandwidth of a radio telescope is usually narrow, the distribution of the intrinsic peak frequency ν_0 of an FRB repeater could be approximately assumed to be uniform near the telescope's bandwidth, i.e., the distribution function of ν_0 could be approximately described by

$$f(\nu_0) \sim \text{const}. \quad (7)$$

We make a Monte Carlo simulation to generate the distribution of the observed spectral bandwidth $\Delta\nu_{\text{obs}}$ of the radio bursts from an FRB repeater, as shown in Figure 1, and take $\nu_{0,t} = 1.25$ GHz and $\Delta\nu_t = 0.5$ GHz that are consistent with the L band of FAST. For $\Delta\nu/\nu_0 = 0.1$, the observed spectral bandwidth $\Delta\nu_{\text{obs}}$ of most bursts are consistent with the intrinsic ones due to $\Delta\nu < \Delta\nu_t$. For $\Delta\nu/\nu_0 = 1$, since many bursts have $\Delta\nu > \Delta\nu_t$, the observed spectral bandwidth $\Delta\nu_{\text{obs}}$ of most bursts would be constrained by the bandwidth of the telescope, leading to $\Delta\nu_{\text{obs}} \sim \Delta\nu_t$. Very few bursts

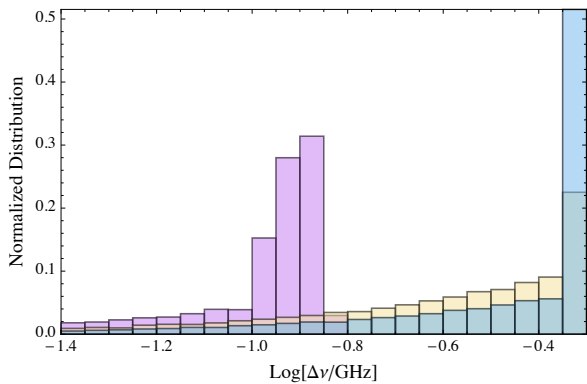


Figure 1. The simulated distribution of the observed spectral bandwidth of radio bursts from an FRB repeater. The purple, yellow, and blue bars correspond to the different relative spectral bandwidths with $\Delta\nu/\nu_0 = 0.1, 0.5$ and 1 , respectively. We take $\nu_{0,t} = 1.25$ GHz and $\Delta\nu_t = 0.5$ GHz for the telescope's parameters. The intrinsic peak frequencies ν_0 of the radio bursts are assumed to be uniformly distributed near the telescope's bandwidths, i.e., $f(\nu_0) = \text{const}$.

have $\Delta\nu_{\text{obs}} < \Delta\nu_t$, because only a part of one end (low-frequency end or high-frequency end) of the intrinsic spectral bandwidth $\Delta\nu$ is within the telescope's bandwidth. Considering that many radio bursts are incomplete in the frequency domain due to the narrow telescope's bandwidth, the observed spectral bandwidth distribution of radio bursts from an FRB repeater could be used to test whether most of the bursts' spectra of an FRB source are intrinsically narrow.

2.2. Physical origin of FRB narrow spectra

Next, we generally discuss the possible physical origin of the intrinsic narrow spectra of FRBs. We consider that a finite pulse of electromagnetic wave has the form of $\vec{E}(t) = \vec{E}_{\parallel}(t) + \vec{E}_{\perp}(t)$, where $\vec{E}_{\parallel}(t)$ and $\vec{E}_{\perp}(t)$ are a pair of orthogonal components of $\vec{E}(t)$. The properties of $\vec{E}(t)$ vary with time and vanishes sufficiently rapidly for $t \rightarrow \pm\infty$, and the power spectrum of $\vec{E}(t)$ satisfies $|E(\omega)|^2 = |E_{\parallel}(\omega)|^2 + |E_{\perp}(\omega)|^2$. Since the two orthogonal components are independent, let us treat only one of the two components, $\vec{E}_k(t)$ with $k = \parallel, \perp$. In particular, if an observed spectrum $|E(\omega)|^2$ appears narrow, the main component between $|E_{\parallel}(\omega)|^2$ and $|E_{\perp}(\omega)|^2$ must also be narrow.

Without loss of generality, the spectrum of the main component could be roughly described by a rectangular profile with a central frequency $\omega_{0,k}$ and a spectral bandwidth $\Delta\omega_k$,

$$|E_k(\omega)|^2 \propto \text{rect}\left(\frac{\omega - \omega_{0,k}}{\Delta\omega_k}\right), \quad (8)$$

where $\text{rect}(x)$ is the rectangular function that is defined as $\text{rect}(x) = 1$ for $|x| \leq 1/2$ and $\text{rect}(x) = 0$ for $|x| >$

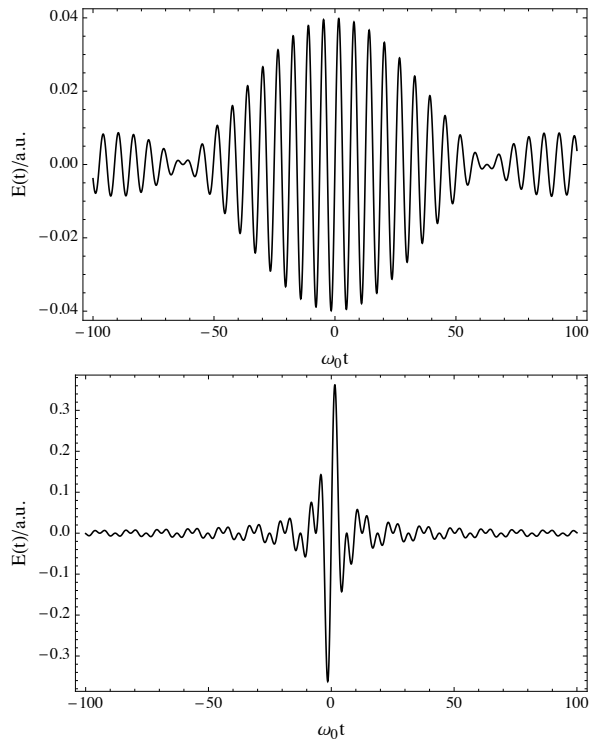


Figure 2. The evolution of electric field component of a pulse of electromagnetic wave with a rectangular power spectrum given by Eq.(8). The top and bottom panels correspond to the scenarios with a narrow spectrum of $\Delta\omega_k/\omega_{0,k} = 0.1$ and with a wide spectrum of $\Delta\omega_k/\omega_{0,k} = 1$, respectively. The phase argument is taken as $\phi_k = 0$ here.

$1/2$. Thus, $E_k(\omega)$ as the Fourier transformation of $E_k(t)$ is given by

$$E_k(\omega) \propto \text{rect}\left(\frac{\omega - \omega_{0,k}}{\Delta\omega_k}\right) e^{i\phi_k}, \quad (9)$$

where ϕ_k is a phase argument. Generally, ϕ_k cannot be directly obtained only based on the information of the power spectrum $|E_k(\omega)|^2$, but for a selected appropriate pair of orthogonal components, $E_{\parallel}(\omega)$ and $E_{\perp}(\omega)$ might be a pair of real and imaginary numbers, i.e., $\text{Im}[E_{\parallel}(\omega)] = E_{\parallel}(\omega)$ and $\text{Re}[E_{\perp}(\omega)] = E_{\perp}(\omega)$, see the following discussions in Section 3.1 and Section 3.2, leading to $\phi_k(\omega) = n\pi/2$ with $n \in \mathbb{Z}$. In this case, one may take $\phi_k = \text{const}$. According to the properties of the Fourier transform, the corresponding pulse profile is

$$E_k(t) \propto \frac{\Delta\omega_k}{\sqrt{2\pi}} \text{sinc}\left(\frac{\Delta\omega_k t}{2}\right) e^{-i(\omega_{0,k} t - \phi_k)}, \quad (10)$$

where $\text{sinc}(x) \equiv \sin x/x$. In Figure 2, we plot the pulse profile $E_k(t)$ based on Eq.(10). The top panel shows the scenario with a narrow spectrum of $\Delta\omega_k/\omega_{0,k} = 0.1$ and the bottom panel shows the scenario with a wide spec-

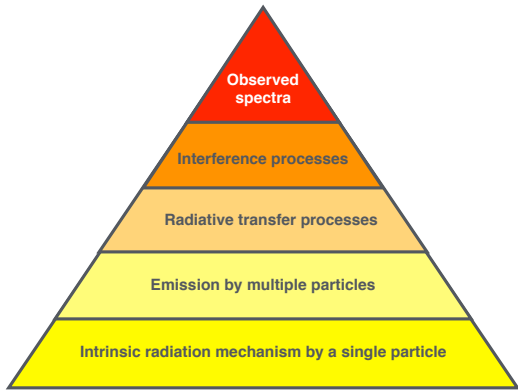


Figure 3. The schematic pyramid illustrates the physical processes affecting the observed spectral features.

trum of $\Delta\omega_k/\omega_{0,k} = 1$. We can see that¹ a narrow spectrum with $\Delta\omega_k/\omega_{0,k} \ll 1$ implies that *the electromagnetic signal $E_k(t)$ should be periodic and quasi-sinusoid with an oscillating frequency of $\omega \sim \omega_{0,k}$ in a short term and have a typical pulse duration of $T \sim 4\pi/\Delta\omega_k$ in a long term.* This conclusion is natural because a narrow spectrum means that the radiation should be quasi-monochromatic, leading to a quasi-sinusoid periodic waveform of $E_k(t)$. In particular, if the periodic quasi-sinusoid signal $E_k(t)$ is produced by the intrinsic radiation mechanism of a single charged particle, and the particle’s acceleration is required to be periodic during its radiation beam pointing to the observer, see the discussion in Section 3.2 and Appendix A.2.

In general, the observed spectral features of an astrophysical phenomenon mainly depend on the following physical processes from the fundamental level to the highest level, see Figure 3:

(1) The most fundamental level is the intrinsic radiation mechanism by a single charged particle that determines the initial radiation of each particle in the emission region. Since the radiating particles in one emission region usually have different energies, in most astrophysical phenomena, the information on the intrinsic radiation mechanism is directly reflected by the spectral shape at the lowest band that is contributed by the particles with the lowest energies.

¹ Notice that although the spectrum by Eq.(8) is assumed to be a rectangular profile here for analytical analysis, this conclusion is widely applicable to other spectral profiles. For example, if the spectrum is described by a Gaussian profile with a peak frequency $\omega_{0,k}$ and a scatter of $\Delta\omega_k$, the corresponding electromagnetic signal would also be periodic and quasi-sinusoid with a frequency of $\omega \sim \omega_{0,k}$ in a short term and have a typical pulse duration of $T \sim 4\pi/\Delta\omega_k$ in a long term, which could be easily tested via the numerical calculation of the corresponding Fourier transform.

(2) The second level is the total emission by all radiating particles in the emission region, which determines the emission coefficient of the emission system. There are two scenarios in this level: incoherent radiation and coherent radiation. For incoherent radiation, the radiation spectral power is just a simple summation of the spectral power of each particle. In this case, due to a wide distribution of the parameters of multiple particles, the relative spectral bandwidth $\Delta\nu/\nu_0$ should be at least wider than that of the intrinsic radiation mechanism by a single particle. However, for coherent radiation, because of the superposition of electromagnetic waves at certain frequencies, the total spectral shape not only depends on the intrinsic radiation mechanism by a single particle but also depend on the specific coherent process in the emission region.

(3) The third level corresponds to the radiative transfer processes, which involves absorption² and scattering. Due to these radiative transfer processes, the incident emission by radiating particles would be changed by absorption or scattering in certain regions. In particular, the absorption processes (e.g., free-free absorption, plasma absorption, synchrotron self-absorption, etc.) usually make the spectra harder, leading to a significant cutoff at the low-frequency band. The frequency-independent electron scattering processes simultaneously suppress the radiation power in all bands, thus, the spectral shape keeps unchanged.

(4) The highest level is the interference processes that change the radiation spectra via the wave interference at a large-scale region, including scintillation, gravitational lensing, plasma lensing, etc. These interference processes might occur in the FRB environments (e.g., circumburst medium, companion wind in a binary system, etc.) or at some regions far away from the FRB sources (e.g., interstellar medium, intergalactic medium, etc.).

In the following sections, we will analyze the above processes in detail and discuss the corresponding implications for the FRB observation.

3. RADIATION SPECTRA BY A SINGLE CHARGED PARTICLE

We first discuss the spectral features of the intrinsic radiation mechanisms by a single charged particle, as the fundamental level pointed out above. The radiation of a

² If the particles have inverted population, the absorption coefficient would become negative, in which case, rather than decrease along ray, the intensity actually increases, so-called as “maser”. However, since the maser mechanism is also one of the main coherent radiation mechanisms, we particularly classify it as the second level in this paper.

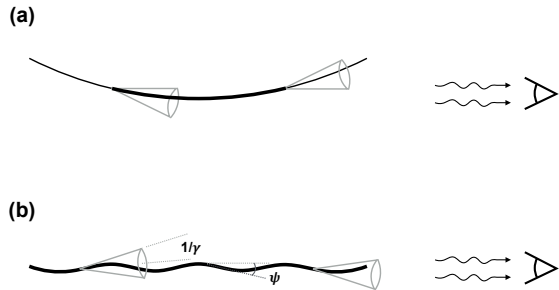


Figure 4. Emission from various points along the trajectory of a relativistic particle. Panel (a) $\gamma\psi \gg 1$: the emission from some parts (bold portions) of the trajectory is observable. Panel (b) $\gamma\psi \ll 1$: the emission from the entire trajectory is observable.

single charged particle with Lorentz factor γ undergoing arbitrary accelerated motion is a coherent superposition with the contributions from the accelerations parallel to and perpendicular to the particle's velocity. For comparable parallel and perpendicular forces, the radiation from the parallel component is of order $1/\gamma^2$ compared to that from the perpendicular component. Thus, one usually neglects the parallel acceleration³. The radiation spectrum of the perpendicular component depends on the relation between the particle's deflection angle ψ and the radiation beaming angle $\sim 1/\gamma$ (Landau & Lifshitz 1975), as shown in Figure 4. The particle's deflection angle ψ is determined as follows. The particle's momentum is $p \sim \gamma m_e c$, and the change in the perpendicular momentum due to a transverse force F_\perp is $p_\perp \sim F_\perp \Delta t_{\text{acc}}$ (Δt_{acc} is the time during which the particle acceleration changes significantly). Thus, the particle's deflection angle is

$$\psi \sim \frac{p_\perp}{p} \sim \frac{F_\perp \Delta t_{\text{acc}}}{\gamma m_e c}, \quad \text{leading to} \quad \gamma\psi \sim \frac{F_\perp \Delta t_{\text{acc}}}{m_e c}. \quad (11)$$

If $\gamma\psi \gg 1$, i.e., the particle's deflection angle is much larger than the radiation beaming angle, the observer will see radiation from a short segment of the electron's

trajectory that is nearly parallel to the line of sight, as shown in the panel (a) of Figure 4, which corresponds to the scenarios of curvature radiation (e.g., Jackson 1998; Yang & Zhang 2018a, 2023), traditional (large-pitch-angle) synchrotron radiation (e.g., Ginzburg & Syrovatskii 1969; Jackson 1998; Rybicki & Lightman 1986), etc. If $\gamma\psi \ll 1$, i.e., the particle's deflection angle is much smaller than the radiation beaming angle, the particle's entire trajectory would be seen by the observer, as shown in the panel (b) of Figure 4, which corresponds to the small-pitch-angle synchrotron radiation (e.g., Epstein 1973), jitter radiation (e.g., Medvedev 2000), etc. In the following discussion, we will discuss the case of $\gamma\psi \gg 1$ in Section 3.1 and the case of $\gamma\psi \ll 1$ in Section 3.2.

3.1. Deflection angle larger than radiation beaming angle

The radiation for $\gamma\psi \gg 1$ is equivalent to the radiation by the particle moving instantaneously at constant speed on an appropriate circular path (Jackson 1998), as shown in the panel (a) of Figure 4. We consider that the acceleration curvature radius is ρ , the angle between the line of sight and the trajectory plane is θ , and the radiation angular frequency is ω . The radiation energy per unit frequency interval per unit solid angle is (Jackson 1998)

$$\mathcal{E}_\omega = \frac{3e^2}{4\pi^2 c} \gamma^2 \hat{\omega}^2 (1 + \gamma^2 \theta^2)^2 \left[K_{2/3}^2(\xi) + \frac{1}{1/\gamma^2 \theta^2 + 1} K_{1/3}^2(\xi) \right]. \quad (12)$$

where $\xi = (\hat{\omega}/2)(1 + \gamma^2 \theta^2)^{3/2}$, $\hat{\omega} = \omega/\omega_c$, and $\omega_c = 3\gamma^3 c/2\rho$ is the typical radiation frequency.

The radiation spectrum by a single radiating particle with $\gamma\psi \gg 1$ is intrinsically wide (Jackson 1998; Yang & Zhang 2018a), $\Delta\omega/\omega_0 \sim 1$, as discuss in Appendix A.1 in detail, and it satisfies the power-law distribution with $\mathcal{E}_\omega \propto \hat{\omega}^{2/3}$ at the low frequency and appears an exponential decay at the high frequency. Therefore, the observed narrow spectrum of FRBs can not be attributed to the intrinsic radiation mechanism by a single charged particle with $\gamma\psi \gg 1$ (also see Katz (2018) for a detailed discussion).

The polarization properties for the scenario of $\gamma\psi \gg 1$ are discussed in Appendix A.1. For the radiation by a single charged particle, the intrinsic linear/circular polarization degree mainly depends on the angle between the viewing direction and the trajectory plane. The larger the viewing angle, the lower (higher) the linear (circular) polarization degree. Besides, the higher the observed frequency, the lower (higher) the linear (circular) polarization degree. Therefore, the high circular

³ However, we should notice that the parallel acceleration could be dominant under the scattering process. For example, if the incident electromagnetic wave is linear polarized and weak (the Lorentz force by the magnetic field component is much weaker than the electric field force), the charged particle would be linearly accelerated by the oscillating electric field (the scenario for strong wave could be seen in Yang & Zhang (2020)). Besides, under the magnetosphere of a neutron star, even if the incident wave is circularly polarized or strong, the charged particle can only oscillate along the field lines due to the existence of a strong background magnetic field and emit the scattering wave due to the parallel acceleration (Beloborodov 2022; Zhang 2022a; Qu & Zhang 2023).

polarization degree should be attributed to the off-beam observation. If there are multiple radiating particles uniformly distributed in a fan beam, the cumulative distributions of the linear and circular polarization degrees would depend on the telescope's sensitivity, the particles' beaming angle and the observed frequency. Important conclusions for the cumulative polarization distributions include: (1) The higher the telescope's sensitivity, the lower the number fraction between the linearly and circularly polarized bursts. The reason is the bursts at larger viewing angles have higher circular polarization degrees and lower fluxes. (2) The larger the particles' beaming angle, the higher the number fraction between the linearly and circularly polarized bursts. If the viewing angle is much larger than $1/\gamma$, most bursts would have high linear polarization. (3) The higher the observed frequency, the higher the number fraction between the linearly and circularly polarized bursts. The reason is that the threshold viewing angle is significantly suppressed at the high frequency, leading to a larger relative number of bursts within the particle beaming angle.

3.2. Deflection angle smaller than radiation beaming angle

In the scenario with $\gamma\psi \ll 1$, the particle with a charge q moves along the line of sight with an almost constant velocity $\vec{\beta}$ but with a varying acceleration $\dot{\vec{\beta}}$ as shown in the panel (b) of Figure 4, which is called a “wiggler” in the laboratory. The radiation energy per unit frequency interval per unit solid angle at the line-of-sight direction \vec{n} could be written as (Landau & Lifshitz 1975, also see Appendix A)

$$\mathcal{E}_\omega = \frac{q^2}{4\pi^2 c} \left(\frac{\omega}{\tilde{\omega}}\right)^4 \left| \vec{n} \times [(\vec{n} - \vec{\beta}) \times \dot{\vec{\beta}}_{\tilde{\omega}}] \right|^2 \quad (13)$$

with

$$\dot{\vec{\beta}}_{\tilde{\omega}} \equiv \int_{-\infty}^{\infty} \dot{\vec{\beta}} e^{i\tilde{\omega}t'} dt' \quad \text{and} \quad \tilde{\omega} \equiv (1 - \vec{n} \cdot \vec{\beta})\omega. \quad (14)$$

where t' is the retarded time. In the ultrarelativistic case, the longitudinal acceleration is smaller than the transverse acceleration, $\dot{\beta}_{\parallel}/\dot{\beta}_{\perp} \sim 1/\gamma^2 \ll 1$. Thus, $\dot{\vec{\beta}}$ and $\vec{\beta}$ are approximately perpendicular to each other, $\dot{\vec{\beta}} \perp \vec{\beta}$. Considering that Fourier component $\dot{\vec{\beta}}_{\tilde{\omega}}$ is significantly different from zero only if $1/\tilde{\omega}$ is of the same order as the time Δt_{acc} during which the particle acceleration changes significantly, the typical frequency of the radiation is estimated to be (Landau & Lifshitz 1975):

$$\omega \sim (1 - \beta)^{-1} \Delta t_{\text{acc}}^{-1} \sim 2\gamma^2 \Delta t_{\text{acc}}^{-1}. \quad (15)$$

For example, if the particle's acceleration is due to the Lorentz force by the magnetic field B , one has $\Delta t_{\text{acc}}^{-1} \sim$

$\omega_B = eB/\gamma m_e c$, where ω_B is the cyclotron frequency, leading to the typical radiation frequency to be $\omega \sim \gamma eB/m_e c$.

In many astrophysical scenarios, the perpendicular acceleration of a charged particle is usually attributed to the Lorentz force by magnetic fields. Such a scenario corresponds to the small-pitch-angle synchrotron radiation, also see Appendix A.2 for a detailed discussion. According to Eq.(A43), the radiation power per unit frequency interval per unit solid angle is

$$\mathcal{P}_\omega = \frac{e^2 \gamma^5 \psi^2 \omega_0}{4\pi c} \bar{\omega}^4 \left(1 - \bar{\omega} + \frac{1}{2}\bar{\omega}^2\right) \delta\left(\bar{\omega} - \frac{2}{1 + \gamma^2 \theta^2}\right), \quad (16)$$

where $\bar{\omega} \equiv \omega/\gamma\omega_0$, and ω_0 is the fundamental cyclotron frequency in the rest frame with velocity $\beta \cos \psi$. The radiation only occurs at the direction θ with

$$\gamma\theta = \left(\frac{2}{\bar{\omega}} - 1\right)^{1/2}. \quad (17)$$

Notice that the particle's deflection angle ψ only affects the normalized radiation power but not the typical frequency and the spectral shape. The typical radiation frequency is $\bar{\omega} \sim$ a few (corresponding to $\omega \sim \gamma\omega_0$). According to Eq.(16), for a certain viewing direction $\gamma\theta$, the emission is only at the frequency $\bar{\omega} = 2/(1 + \gamma^2 \theta^2)$. Thus, *the radiation spectrum of a single particle should be extremely narrow*. This result is consistent with the conclusion discussed in Section 2.2, that is, the narrow spectrum could be produced by that the particle's acceleration is periodic during its radiation beam pointing to the observer. If multiple radiating particles are distributed in a three-dimensional beam, the corresponding spectrum would become relatively wider than that of a single charged particle, but the spectrum is still narrow with $\Delta\nu/\nu \ll 1$, see Appendix A.2 for a detailed calculation. Therefore, if the observed narrow spectrum of FRBs is due to the intrinsic radiation mechanism by a single charged particle, it should be attributed to the scenario of $\gamma\psi \ll 1$.

The polarization properties for the scenario of $\gamma\psi \ll 1$ are discussed in Appendix A.2. First, for the general polarization properties of the scenario with $\gamma\psi \ll 1$, it can be easily proved that (1) If the acceleration is always on a straight line perpendicular to the particle's velocity, the polarization is fully linear; (2) If the acceleration rotates with a constant angular velocity on the plane perpendicular to the particle's velocity, the polarization is fully circular. In particle, for the small-pitch-angle synchrotron radiation by a single charged particle, high linear polarization (low circular polarization) only occur

at $\bar{\omega} \sim 1$ and $\gamma\theta \sim 1$, otherwise, high circular polarization (low linear polarization) is dominant. For multiple radiating particles uniformly distributed in a three-dimensional beam, the observed linear and circular polarization degrees depend on the gyration directions of the radiating particles and whether the viewing direction is within the beaming angle. If all radiating particles have the same gyration directions, the polarization of this radiation mechanism would be almost 100% circular polarization, otherwise, their polarizations would cancel out.

3.3. Different astrophysical scenarios

The above two general radiation processes with $\gamma\psi \gg 1$ and $\gamma\psi \ll 1$ could appear in various astrophysical scenarios, e.g. in the magnetosphere of a neutron star or in a magnetized shocked medium. The radiation processes in the magnetosphere are shown in Figure 5. In the inner region of the magnetosphere, due to the strong magnetic field, the electrons move almost along the curvature field lines and produce curvature radiation⁴. In the picture of the curvature radiation, since the deflection angle (i.e., the deflection angle of the field line) is much larger than the radiation beaming angle, the condition of $\gamma\psi \gg 1$ is satisfied. In the outer region of the magnetosphere with the relatively weak magnetic field, the electrons would move in the field lines with a spiral trajectory and the corresponding radiation mechanism is the small-pitch-angle synchrotron radiation. The deflection angle ψ in this case corresponds to the pitch angle of the synchrotron radiation, leading to $\gamma\psi \ll 1$. One should notice the difference in the deflection angles ψ in the above two scenarios due to the different mechanisms.

The critical conditions between the curvature radiation and the small-pitch-angle synchrotron radiation could be obtained as follows: when a charged particle with a Lorentz factor γ moving along a trajectory with a curvature radius of ρ , the observer will see the radiation with the emission cone of angular width $1/\gamma$ around the observer direction and the typical timescale of the radiating process is $\tau_r = \rho/\gamma c$. The gyration period of an electron under a magnetic field is $\tau_B = 2\pi/\omega_B = 2\pi\gamma m_e c/eB$. If the radiation process is dominated by the small-pitch-angle synchrotron, the number of times for the electron's gyration during the time of τ_r must be much larger than once, which requires that the gyration period of the electron is much shorter than τ_r , $\tau_B < \tau_r$,

⁴ The accelerations of the electrons are essentially by the Lorentz forces of the drift velocities perpendicular to the field lines.

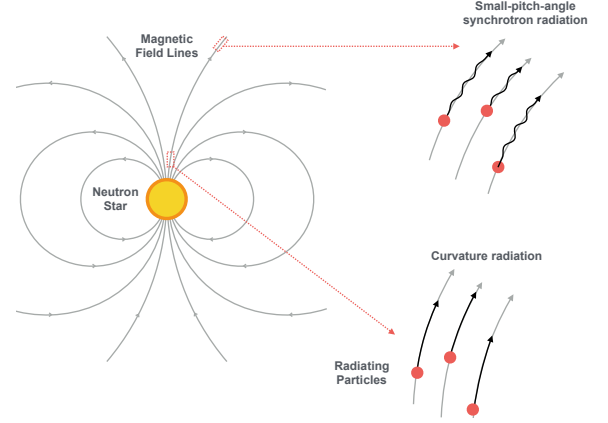


Figure 5. Two radiation mechanisms with $\gamma\psi \gg 1$ and $\gamma\psi \ll 1$ in the magnetosphere of a neutron star. In the inner region with a relatively strong magnetic field, the radiation mechanism is the curvature radiation. In the outer region with a relatively weak magnetic field, the radiation mechanism is the small-pitch-angle synchrotron radiation.

leading to the first necessary condition:

$$B > B_{\text{cr},1} = \frac{2\pi\gamma^2 m_e c^2}{e\rho} \simeq 1.1 \text{ G } \gamma_2^2 \rho_8^{-1}. \quad (18)$$

According to the Larmor formula, the radiation power of the small-pitch-angle synchrotron radiation is

$$P = \frac{2}{3} \frac{e^4 \gamma^2 B^2 \beta_{\perp}^2}{m_e^2 c^3} \simeq \frac{2}{3} \frac{e^4 \gamma^2 B^2 \psi^2}{m_e^2 c^3}, \quad (19)$$

where $\beta_{\perp} = \beta \sin \psi \simeq \psi$ for $\beta \sim 1$ and $\psi \ll 1$. The cooling timescale is estimated by $P t_{\text{cool}} \sim \gamma m_e c^2$, and one obtains

$$t_{\text{cool}} \sim \frac{3m_e^3 c^5}{2e^4 \gamma B^2 \psi^2} \simeq 5.2 \times 10^{10} \text{ s } \gamma_2^{-1} B_1^{-2} \psi_{-3}^{-2}. \quad (20)$$

If the small-pitch-angle synchrotron radiation is not significantly cooling during the electron moving along the field line, the cooling timescale t_{cool} must be larger than τ_r , leading to the second necessary condition:

$$B < B_{\text{cr},2} = \left(\frac{3m_e^3 c^5}{2e^4 \rho \psi^2} \right)^{1/2} \simeq 3.9 \times 10^8 \text{ G } \rho_8^{-1/2} \psi_{-3}^{-1}. \quad (21)$$

Based on Eq.(18) and Eq.(21), the small-pitch-angle synchrotron radiation finally requires the conditions:

$$1.1 \text{ G } \gamma_2^2 \rho_8^{-1} \lesssim B \lesssim 3.9 \times 10^8 \text{ G } \rho_8^{-1/2} \psi_{-3}^{-1}. \quad (22)$$

Accordingly, the condition of the curvature radiation is

$$B \gtrsim 3.9 \times 10^8 \text{ G } \rho_8^{-1/2} \psi_{-3}^{-1}. \quad (23)$$

As we expected, the small-pitch-angle synchrotron radiation is preferred to be in the outer region of the magnetosphere, and the curvature radiation is preferred to be in the inner region of the magnetosphere.

Next, we make some comments about the observable properties of the small-pitch-angle synchrotron radiation in the magnetosphere. As discussed in Section 3.2, according to Eq.(15) the typical radiation frequency of the small-pitch-angle synchrotron radiation is

$$\nu \sim \gamma^2 \nu_B = \frac{\gamma e B}{2\pi m_e c} \simeq 2.8 \text{ GHz } \gamma^2 B_1. \quad (24)$$

Thus, the small-pitch-angle synchrotron radiation in the outer magnetosphere could be emitted at the GHz band⁵. The polarization properties of the small-pitch-angle synchrotron radiation depend on the gyration motions of the charged particles in the magnetosphere, see the following discussions in Appendix A.2. Before the charged particles enter the magnetosphere's outer region, in addition to the parallel velocities along the field line, the charged particles have a small drift velocity perpendicular to the field lines, providing an additional Lorentz force to make the particles move along the curved paths. Since the direction of the drift velocity only depends on the curved field line, the charged particles tend to have the same gyration direction when they enter the outer region of the magnetosphere. Thus, the small-pitch-angle radiation is expected to be highly circularly polarized (see Appendix A.2). Besides, since the spectral shape and the typical frequency of the small-pitch-angle radiation is independent of the particle's pitch angle, for multiple particles, the spectral bandwidth is mainly determined by the distribution of the particles' Lorentz factors.

The above two general radiation processes with $\gamma\psi \gg 1$ and $\gamma\psi \ll 1$ might also occur in the magnetized shocked medium, which corresponds to the traditional synchrotron radiation and small-pitch-angle synchrotron radiation, as shown in the panel (a) and the panel (b) of Figure 6. The critical condition between the two scenarios depends on the relative directions between the

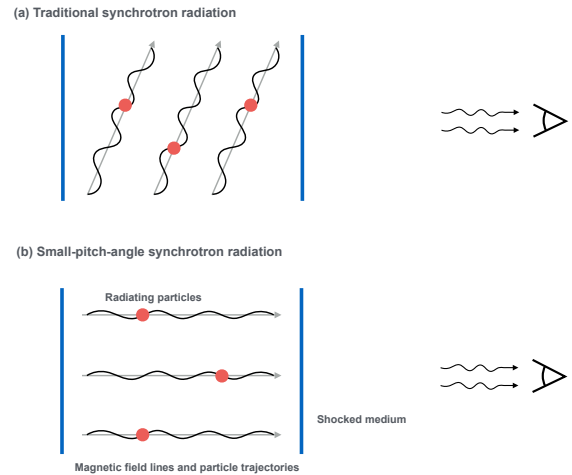


Figure 6. Two radiation mechanisms with $\gamma\psi \gg 1$ and $\gamma\psi \ll 1$ in the magnetized shocked medium. Panel (a) corresponds to traditional synchrotron radiation. Panel (b) corresponds to the small-pitch-angle synchrotron radiation, in which scenario, the emission region has a magnetic field almost parallel to the line of sight and the direction of the particles' injection is almost parallel to the field lines.

magnetic field, the particles' injection, and the viewing direction. If the direction of the particles' injection is almost parallel to the field lines, the radiation mechanism would be the small-pitch-angle synchrotron radiation, as shown in the panel (b) of Figure 6. However, due to the shock compression, the magnetic field in the shocked medium usually has a significant component parallel to the shock surface. Thus, the small-pitch-angle injection process seems to be fine-tuning. Besides, in the magnetized shocked medium, since the directions of the particles' gyration motion are random, the small-pitch-angle synchrotron would be significantly depolarized for multiple particles.

4. RADIATION SPECTRA BY COHERENT PROCESSES OF MULTIPLE PARTICLES

In this section, we discuss how the coherent processes generate narrow spectra, including the bunching mechanism (Section 4.1) and maser mechanism (Section 4.2).

4.1. Narrow spectra by bunching mechanism

Coherent curvature radiation by charged bunches has been proposed as one of the popular ideas to explain the emission of FRBs (e.g., Katz 2014, 2018; Yang & Zhang 2018a, 2023; Kumar & Bošnjak 2020; Lu et al. 2020; Cooper & Wijers 2021). Compared with the spectrum by a single charged particle with $\gamma\psi \gg 1$, see Section 3.1 and Figure 10, a relatively narrow spectrum could be generated by the coherent curvature radiation from a structured bunch as proposed by Yang et al. (2020) and

⁵ Notice that the typical frequency at GHz band requires the magnetic field to be $B \sim 10$ G according to Eq.(24). Such a weak field strength leads to the local magnetic energy density being much smaller than the plasma energy density, $B^2/8\pi \ll \xi^{-1} L_{\text{iso}}/4\pi r^2 c$, where L_{iso} is the isotropic luminosity of an FRB and ξ is the radiation efficiency. This means that the radiating particles will straighten the field lines (that is similar to the magnetic field geometry of stellar wind), leading to a larger curvature radius ρ than that of the dipole field at the same position. Such a process makes the small-pitch-angle radiation easy to produce because the field lines become almost parallel to the particles' velocities. However, how to generate coherent radiation is an issue for such a scenario, which need to be further analyzed in detail.

Yang & Zhang (2023) because the frequency structure of the burst is the Fourier transform of the spatial structure of the radiating charge density as pointed out by Katz (2018), but it is still hard to explain the observed extremely narrow spectrum of some FRBs, e.g., FRB 20190711 with $\Delta\nu/\nu \sim 0.05$. In particular, the dynamic fluctuation of the bunches would also make the spectrum show a white noise, especially at the low-frequency band (Yang & Zhang 2023). Since the narrow spectrum implies that the electromagnetic signal should be quasi-sinusoid in the short term as pointed out in Section 2.2, one possibility to generate a narrow spectrum is that the radiating bunches moving along the same trajectory are quasi-periodically distributed due to some special processes, like quasi-monochromatic Langmuir wave or oscillating pair creation in the charge-starved region. In this case, the radiation could be amplified at some harmonic frequencies, see the following discussion.

We consider that the charged bunch distribution is quasi-periodic in the time domain, and the medium in the emission contains N radiating bunches. Each radiating bunch emits a pulse of $E_0(t)$ with the same shape but with different arrival times. Thus, the total electric field from the multiple radiating bunches is given by

$$E(t) = \sum_j^N E_0(t - t_j). \quad (25)$$

According to the time-shifting property of the Fourier transform, the total power spectrum of multiple radiating bunches is

$$|E(\omega)|^2 = |E_0(\omega)|^2 \left| \sum_j^N e^{i\omega t_j} \right|^2, \quad (26)$$

where $|E_0(\omega)|^2$ corresponds to the power spectrum of the first radiating bunch. The coherence properties of the radiation by the multiple bunches are determined by the factor of $|\sum_j^N \exp(i\omega t_j)|^2$. If the multiple bunches are quasi-periodically distributed, one would have

$$i\omega t_j = ij\omega/\omega_m + i\delta\phi_j, \quad (27)$$

where $1/\omega_m = \text{const.}$ corresponds to the period of the bunch distribution, and $\delta\phi_j$ corresponds to the relative random phase related to the phase of $j\omega/\omega_m$.

We first consider the case of $\delta\phi_j = 0$, which implies that the bunch distribution is strictly periodic. Defining $z = \exp(i\omega/\omega_m)$, the modulus square of the sum of the

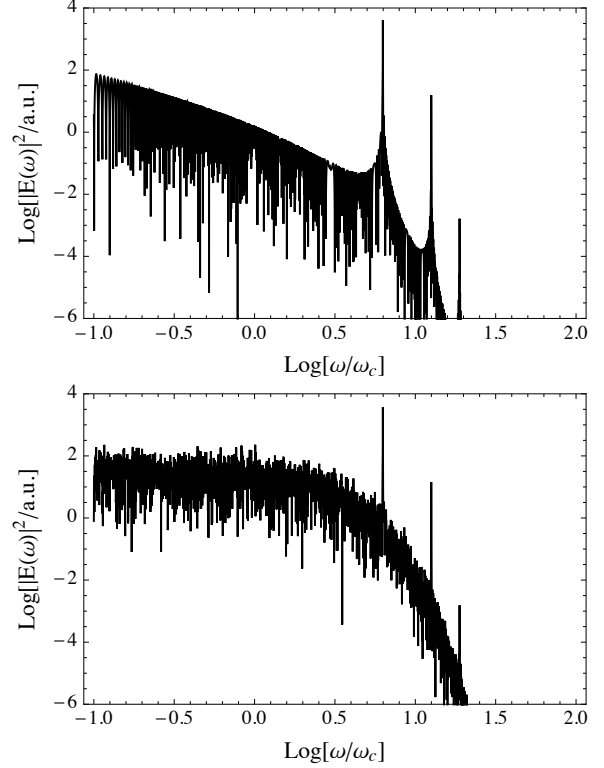


Figure 7. The spectra of multiple radiating bunches with a periodic or quasi-periodic distribution in the time domain. The top panel corresponds to a strictly periodic distribution with $\delta\phi_j = 0$. The bottom panel corresponds to a quasi-periodic distribution with $\delta\phi_j$ uniformly distributed in $[-0.5, 0.5]$. A curvature-radiation-like spectrum for a single point-source bunch, $|E_0(\omega)|^2 \propto \omega^{2/3} \exp(-\omega/\omega_c)$, is taken as an example in this figure. We take $\omega_m = \omega_c$ and $N = 10^3$. The peak frequency is at $2n\pi\omega_m$ with $n \in \mathbb{Z}^+$.

phase factor in Eq.(26) is calculated by

$$\begin{aligned} \left| \sum_{j=1}^N z^j \right|^2 &= \left| z \frac{z^N - 1}{z - 1} \right|^2 = \frac{2 - z^N - z^{*N}}{2 - z - z^*} \\ &= \frac{1 - \cos(N\omega/\omega_m)}{1 - \cos(\omega/\omega_m)} = \frac{\sin^2(N\omega/2\omega_m)}{\sin^2(\omega/2\omega_m)}, \end{aligned} \quad (28)$$

where z^* is the conjugation of the complex number z , and the geometric sequence summation is used in the above calculation. Therefore, the power spectrum by the multiple bunches with a periodic distribution is given by

$$|E(\omega)|^2 = |E_0(\omega)|^2 \sin^2\left(\frac{N\omega}{2\omega_m}\right) \sin^{-2}\left(\frac{\omega}{2\omega_m}\right). \quad (29)$$

The radiation is coherently amplified when $\sin^2(\omega/2\omega_m) \sim 0$, leading to the coherent peak frequencies at $\omega/\omega_m = 2n\pi$ with $n \in \mathbb{Z}^+$. In the top panel of Figure 7, we plot the power spectrum of the multiple radiating bunches with a periodic distribution according

to Eq.(29). The spectrum of a single bunch is assumed to be $|E_0(\omega)|^2 \propto \omega^{2/3} \exp(-\omega/\omega_c)$ (corresponding to the spectrum of the curvature radiation by a single point-source bunch, see Yang & Zhang (2018a, 2023)) as an example, and $N = 10^3$ and $\omega_m = \omega_c$ are taken. We can see that the coherent radiation energy is radiated into multiples of $2\pi\omega_m$ with narrow bandwidths.

Next, we consider that the bunch distribution is quasi-periodical with $\delta\phi_j \neq 0$. We assume that the relative random phases $\delta\phi_j$ are uniformly distributed in a range of $[-\delta\phi_m, \delta\phi_m]$ with $0 < \delta\phi_m \leq \pi$, and make a Monte Carlo simulation to calculate the total radiation based on Eq.(26) and Eq.(27). In the bottom panel of Figure 7, we plot the power spectrum of the multiple radiating bunches with a quasi-periodic distribution with $\delta\phi_m = 0.5$. The other parameters are the same as that in the case of strictly periodic distribution. We can see that the coherent radiation energy is still radiated into multiples of $2\pi\omega_m$ with narrow bandwidths even for $\delta\phi_j \neq 0$. Meanwhile, for a given frequency band, the continuous part of the spectrum becomes harder for a larger value of $\delta\phi_m$. In particular, if $\delta\phi_m = \pi$, the distribution of the multiple bunches would be random and the total power spectrum completely incoherent.

4.2. Narrow spectra by maser mechanism

In addition to the bunching mechanism, some maser mechanisms have been also proposed to be the radiation mechanism of FRBs (e.g., Lyubarsky 2014; Metzger et al. 2019; Waxman 2017; Beloborodov 2020). The maser mechanism corresponds to the negative absorption by radiating particles with inverted populations. A negative optical depth of τ_ν at frequency ν causes an amplification by a factor of

$$A(\nu) = \exp(|\tau_\nu|). \quad (30)$$

Thus, the amplification involved in the maser mechanism could be very large even for an intermediate negative optical depth.

We first consider that the electron distribution (i.e., the electron number density in an interval of $(\gamma, \gamma + d\gamma)$ with γ as the electron Lorentz factor) is

$$n(\gamma)d\gamma \propto \gamma^p d\gamma, \quad (31)$$

the radiation power of a single electron is $P(\nu, \gamma)$, and the scale of the emission region is L . The optical depth

τ_ν could be generally given by⁶ (e.g., Rybicki & Lightman 1986)

$$\tau_\nu = -\frac{L}{8\pi m_e \nu^2} \int P(\nu, \gamma) \left[\gamma^2 \frac{\partial}{\partial \gamma} \left(\frac{n(\gamma)}{\gamma^2} \right) \right] d\gamma. \quad (32)$$

Thus, the negative absorption requires that $\tau_\nu < 0$, i.e., $\partial(n(\gamma)/\gamma^2)/\partial\gamma > 0$, leading to the condition of

$$p > 2. \quad (33)$$

In general, the electron distribution $n(\gamma)$ in the emission is usually wide and appears more complex than a single power-law distribution given by Eq.(31), that is, the power-law index p could be energy-dependent, $p(\gamma)$. In this case, the effective electrons contributing to the maser mechanism are only in the range in which $p(\gamma) > 2$. We rewrite Eq.(32) as

$$\tau_\nu = \tau_{\nu,+} + \tau_{\nu,-}, \quad (34)$$

where $\tau_{\nu,+}$ and $\tau_{\nu,-}$ are the positive and negative optical depths with the integral ranges in Eq.(32) corresponding to $p(\gamma) < 2$ and $p(\gamma) > 2$, respectively. For an effective maser mechanism, one usually has $|\tau_{\nu,-}| \gg \tau_{\nu,+}$ and $\tau_\nu \simeq \tau_{\nu,-}$ unless the electron distribution is very fine-tuning leading to a small net negative absorption. Thus, in the following discussion, we only consider the electrons distributed in

$$\gamma_{\min} < \gamma < \gamma_{\max} \quad \text{in which range } p(\gamma) \sim p > 2, \quad (35)$$

where $p(\gamma_{\min}) = p(\gamma_{\max}) \simeq 2$.

We are mainly interested in the synchrotron maser that has been proposed as one of the popular ideas to explain the coherent emission of FRBs (e.g., Lyubarsky 2014; Metzger et al. 2019; Waxman 2017; Beloborodov 2020). The δ -function approximation for the synchrotron emissivity can be written as

$$\begin{aligned} P(\nu, \gamma) &\simeq \frac{4}{3} c \sigma_T \frac{B^2}{8\pi} \gamma^2 \delta(\nu - \gamma^2 \nu_B) \\ &= \frac{4\pi}{9} \frac{e^3 B}{m_e c^2} \gamma \delta \left(\gamma - \sqrt{\frac{\nu}{\nu_B}} \right), \end{aligned} \quad (36)$$

⁶ Notice that this equation is very general because it is directly derived from Einstein coefficient. However, we should emphasize that this equation potentially assumes that the electron distribution is isotropic. If the electron distribution is one-dimensional (e.g., relativistic electrons and positrons moving along the magnetic field lines in the magnetosphere of a neutron star), the integrand in Eq.(32) would be proportional to $dn(\gamma)/d\gamma$ (Melrose 1978) rather than $\gamma^2 \partial[n(\gamma)/\gamma^2]/\partial\gamma$, and the condition for the negative absorption would become $p > 0$ rather than $p > 2$.

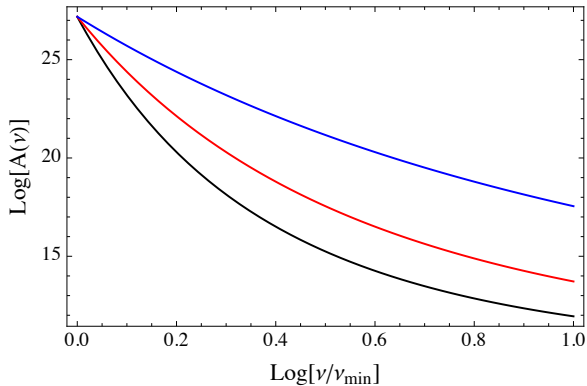


Figure 8. The amplification of the synchrotron maser mechanism as a function of frequency. The black, red and blue lines correspond to the electron distribution index $p = 2.5, 3, 3.5$, respectively. The optical depth at ν_{\min} is assumed to be $\tau_{\nu,0} = 10$ here. The frequency is dimensionless with $\nu_{\min} = \gamma_{\min}^2 \nu_B$. Notice that the amplification becomes zero for $\nu < \nu_{\min}$ in this figure, see the text for the discussion.

where $\nu_B = eB/2\pi m_e c$ is the cyclotron frequency. Substituting Eq.(31) and Eq.(36) in Eq.(32) gives

$$\begin{aligned} \tau_\nu &\sim \frac{e^3 B L}{18 m_e^2 c^2} \frac{n(\gamma \sim \sqrt{\nu/\nu_B})}{\nu^2} \\ &\propto \nu^{(p-4)/2}. \quad \text{for } \gamma_{\min}^2 \nu_B < \nu < \gamma_{\max}^2 \nu_B. \end{aligned} \quad (37)$$

Based on Eq.(30) and Eq.(37), we take the form of amplification as $A(\nu) = \exp[\tau_{\nu,0}(\nu/\nu_{\min})^{(p-4)/2}]$, where $\tau_{\nu,0}$ corresponds to the optical depth at $\nu_{\min} = \gamma_{\min}^2 \nu_B$ and $2 < p < 4$ is assumed. In Figure 8, we plot the spectra of the synchrotron maser, and an intermediate optical depth of $\tau_{\nu,0} = 10$ is assumed. The black, red, and blue lines correspond to $p = 2.5, 3, 3.5$, respectively. We can see that for these typical parameters, the amplification varies several orders of magnitude within a narrow bandwidth. Thus, the spectrum of synchrotron maser should be extremely narrow.

5. RADIATION SPECTRA CORRECTED BY RADIATIVE TRANSFER PROCESSES

The radiative transfer processes include absorption (Section 5.1) and scattering (Section 5.2). Since both absorption and scattering are dominant in some dense environments, they are important only at the circumburst medium or the emission region.

5.1. Absorption

The absorption coefficients α_ν of most absorption processes (e.g., free-free absorption, synchrotron absorption, plasma absorption, etc.) have a negative correlation with the frequency of electromagnetic waves, $\alpha_\nu \propto \nu^{-\delta}$ with $\delta > 0$, that is, the lower the frequency,

the more significant the absorption effect. We consider that the incident intensity is $I_{\nu,0}$ and the scale of the absorption region is L , then the outgoing intensity has a spectrum of $I_{\nu,0} \exp(-\alpha_\nu L)$. If the frequency ν is much less than the absorption frequency ν_{abs} defined by $\tau_\nu(\nu_{\text{abs}}) = \alpha_\nu(\nu_{\text{abs}})L = 1$, the intensity would be significantly cut off, i.e., $I_\nu(\nu < \nu_{\text{abs}}) \ll I_{\nu,0}$. This result suggests that the radio bursts emitted during a limited time of T would have the same low-frequency cutoff at $\nu_{\text{low}} \sim \nu_{\text{abs}}$ if the intrinsic spectrum is intrinsically wide and the typical evolution timescale of the absorption parameters is much longer than T . However, such a conclusion is inconsistent with the observations of some FRB repeaters, suggesting that the absorption effects do not significantly change the observed spectra.

For example, FRB 200428 from Galactic magnetar SGR J1935+2154 consisted of two sub-bursts separated by $T \sim 29$ ms (CHIME/FRB Collaboration et al. 2020). The first component did not show a significant low-frequency cutoff at the telescope's bandwidth, implying that the low-frequency cutoff satisfies $\nu_{\text{low}} \ll 400$ MHz, and the second component had a low-frequency cutoff at $\nu_{\text{low}} \sim (400 - 500)$ MHz. The relative variation of the low-frequency cutoffs, $\delta\nu_{\text{low}}/\nu_{\text{low}}$, was several tens percent during $T \sim 29$ ms. This observation suggests that the relative variations of the environment parameters (e.g., average electron density, absorption region lengthscale, temperature, magnetic field, etc.) in the absorption region also reached several tens percent during such an extremely short time, which is obviously not realistic. Therefore, the low-frequency cutoffs of the observed spectra of some FRB sources should not be attributed to the absorption processes.

5.2. Electron Scattering

The most important mechanism of various scatterings is electron scattering, including relativistic and nonrelativistic types. Relativistic electron scattering mainly refers to inverse Compton scattering. For a general large-angle scattering process by a relativistic electron with Lorentz factor of γ , the inverse Compton scattering process converts a photon with frequency ν to a high-frequency one with frequency $\sim \gamma^2 \nu$. Since the cross section (i.e., Thomson cross section) is independent of the photon frequency, the scattering process simultaneously suppresses the specific intensity in all bands, leading to the spectral shape of the unscattered radiation unchanged.

The nonrelativistic electron scattering is called Thomson scattering. As an elastic scattering process, the total amount of radiation emitted per unit frequency is almost equal to the total amount absorbed in that same

frequency and the cross section is also independent of frequency. However, repeating scattering process can build up a substantial effect, i.e., induced Compton scattering⁷. The induced Compton scattering on relatively dense plasma would unavoidably affect the emergent radiation. We consider that the electron number density is n_e , the electron temperature is T , the photon occupation number (i.e, the average number of photons in a state) is (e.g., Rybicki & Lightman 1986; Wilson 1982; Yang & Zhang 2023) $n_\gamma = kT_B/h\nu = (c^2/2h\nu^3)I_\nu$, where T_B is the radiation brightness temperature and I_ν is the radiation intensity. The kinetic equation for the photon interacting with nonrelativistic electrons is (Kompaneets 1957; Syunyaev 1971; Rybicki & Lightman 1986)

$$\frac{\partial n_\gamma}{\partial t} = \frac{h\sigma_T n_e}{m_e c} \frac{1}{\nu^2} \frac{\partial}{\partial \nu} \nu^4 \left(n_\gamma^2 + n_\gamma + \frac{kT}{h} \frac{\partial n_\gamma}{\partial \nu} \right). \quad (38)$$

This is the so-called Kompaneets equation, which describes the evolution of the photon distribution function due to repeated nonrelativistic electron scattering. For FRBs with extremely temperatures, we are only interested in $n_\gamma \gg 1$ (i.e., $kT_B \gg h\nu$) and $n_\gamma \gg kT/h\nu$ (i.e., $T_B \gg T$), leading to the second and third terms in the parentheses ignored. Thus, the kinetic equation could be written as

$$\frac{\partial n_\gamma}{\partial t} = \frac{2h\sigma_T n_e n_\gamma}{m_e c} \frac{\partial(\nu^2 n_\gamma)}{\partial \nu}. \quad (39)$$

According to the above equation, the radiation with the brightness temperature T_B is unable to escape from a region with an effective optical depth $\tau_{\text{ind}} = (kT_B/m_e c^2)\tau_T > 1$ (Lyubarsky & Ostrovska 2016), where τ_T is the optical depth of Thomson scattering. The total number of photons is conserved and the photons are redistributed toward lower frequencies, which leads a larger brightness temperature T_B so that the rate of redistribution increases further out. Finally, the photons are eventually absorbed by some absorption processes, e.g., free-free absorption, synchrotron absorption, plasma absorption, etc. In conclusion, the induced Compton scattering makes the emergent spectrum softer than the initial incident spectrum and cuts off the spectrum at a low frequency determined by the absorption processes. Based on the discussion in Section 5.1, since the radio bursts of an FRB repeater did not show the same low-frequency cutoff during a limited time, the effect of induced Compton scattering should also be ignored.

⁷ Induced Compton scattering could be significant for relativistic electron scattering when the scattering angle is so small that the scattering frequency is close to the incident one.

The above electron scattering mechanisms potentially assume that the scattering processes are linear, which means that the electron oscillation is nonrelativistic and the interaction between electromagnetic wave and electron is dominated by electric force (i.e., Lorentz force could be ignored due to the nonrelativistic motion of electrons). We consider an electromagnetic wave has an electric field E and frequency ω , and define the strength parameter as

$$a = \frac{v_{\text{os}}}{c} = \frac{eE}{2\pi m_e c \nu}, \quad (40)$$

where $v_{\text{os}} = eE/2\pi m_e \nu$ is the typical oscillation velocity due to the electric force. For $a \ll 1$, the electron oscillation is nonrelativistic and the interaction is dominated by the electric force, which means that the Thomson theory is valid. For $a \gg 1$, the electron oscillation becomes relativistic and the interaction between electron and electromagnetic wave enters the nonlinear regime of “strong waves”. In particular, the nonlinear effect makes the cross section enhanced by a factor of a^2 (e.g., Sarachik & Schappert 1970; Yang & Zhang 2020; Beloborodov 2022; Qu et al. 2022)

$$\sigma \sim a^2 \sigma_T \propto \frac{I_\nu}{\nu}, \quad (41)$$

where I_ν is the incident intensity. Thus, the lower the frequency or the high the intensity, the more significant the scattering. According to Eq.(41), the radio bursts would have low-frequency cutoff at $\nu_{\text{low}} \propto I_\nu$, which is worthy to test the nonlinear effect by the observations of FRB repeaters. In addition to the escape unscattered photons, high-frequency photons would be produced by the relativistically oscillating electrons but they are significantly outside the band of the incident photons, which is beyond the scope of this work.

6. RADIATION SPECTRA CORRECTED BY INTERFERENCE PROCESSES

The interference processes that can change the radiation spectra mainly include scintillation, gravitational lensing, and plasma lensing. Due to the wave interference, the spectra are coherently enhanced at some frequencies but coherently reduced at some others frequencies.

6.1. Scintillation

Generally, “scintillation” refers to the spectral modulations caused by the coherent combination of multiple waves, and “temporal scattering” refers to the temporal broadening of pulses due to the multipath propagation. For a certain plasma screen, the relation between

scintillation and temporal scattering is $\Delta\nu_{\text{sci}}\tau_s \sim 1/2\pi$, where $\Delta\nu_{\text{sci}}$ is the scintillation bandwidth and τ_s is the scattering time. If the observed temporal scattering is $\tau_s \sim 1$ ms, the corresponding scintillation bandwidth should be $\Delta\nu_{\text{sci}} \sim 160$ Hz, which is much smaller than the observed scintillation bandwidth of $\Delta\nu_{\text{sci}} \sim 1$ MHz. Therefore, for extragalactic FRBs, the observed scintillation is proposed to be mainly contributed by the interstellar medium within the Milky Way, and the observed scattering time is more likely contributed by the circumburst medium or the interstellar medium in the FRB host galaxy.

In this section, we consider that the spectral shape with a typical bandwidth $\gtrsim 100$ MHz might be attributed to another plasma screen that is different from the regions contributing the observed temporal scattering and the narrow-bandwidth scintillation with $\Delta\nu_{\text{sci}} \sim 1$ MHz. The relatively wider scintillation bandwidth of $\Delta\nu_{\text{sci}} \gtrsim 100$ MHz requires that the screen should be close to the FRB source. We consider that the plasma screen has a thickness of ΔR , and the power spectrum of electron density fluctuations in the plasma screen is power-law with

$$P(k) = C_N^2 k^{-\beta}, \quad \text{for } 2\pi L^{-1} \lesssim k \lesssim 2\pi l_0^{-1}, \quad (42)$$

where β is the spectral index of the three-dimensional power spectrum (Kolmogorov turbulence has $\beta = 11/3$), $k = 2\pi/l$ is the spatial wavenumber, l_0 and L are the inner and outer scales of the inertial range of the turbulence, respectively, and the normalization factor C_N^2 is given by (e.g., Xu & Zhang 2017; Yang et al. 2022)

$$C_N^2 \simeq \begin{cases} \frac{3-\beta}{2(2\pi)^{4-\beta}} l_0^{3-\beta} \delta n_e^2, & \text{for } \beta < 3, \\ \frac{\beta-3}{2(2\pi)^{4-\beta}} L^{3-\beta} \delta n_e^2, & \text{for } \beta > 3, \end{cases} \quad (43)$$

where δn_e^2 is the total mean-squared density fluctuation. We define the diffractive lengthscale l_{diff} that represents the transverse separation for which the root-mean-squared difference of the wave phases is equal to unit rad. For the electromagnetic wave with a wavelength of λ , the diffractive lengthscale l_{diff} is (e.g., Xu & Zhang 2017; Yang et al. 2022)

$$l_{\text{diff}} = \begin{cases} (f_{1,\alpha} \pi^2 r_e^2 \lambda^2 l_0^{\beta-4} C_N^2 \Delta R)^{-\frac{1}{2}}, & \text{for } l_{\text{diff}} < l_0, \\ (f_{2,\alpha} \pi^2 r_e^2 \lambda^2 C_N^2 \Delta R)^{\frac{1}{2-\beta}}, & \text{for } l_{\text{diff}} > l_0, \end{cases} \quad (44)$$

where r_e is the classical electron radius, $f_{1,\alpha} = \Gamma(1 - \alpha/2)$, $f_{2,\alpha} = [\Gamma(1 - \alpha/2)/\Gamma(1 + \alpha/2)](8/\alpha 2^\alpha)$, and $\alpha = \beta - 2$. For the Kolmogorov turbulence with $\alpha = 5/3$ ($\beta = 11/3$), one has $f_{1,\alpha} = 5.6$ and $f_{2,\alpha} = 8.9$, respectively.

The scattering angle of the electromagnetic waves is $\theta_s \simeq \lambda/2\pi l_{\text{diff}}$, and the transverse scale of the visible part of the plasma screen is (e.g., Yang et al. 2022)

$$l_s(\lambda) = \theta_s R \simeq \frac{\lambda R}{2\pi l_{\text{diff}}}, \quad (45)$$

where R is the distance from the plasma screen to the FRB source. The temporal scattering time could be then estimated by

$$\tau_s(\lambda) \simeq \frac{l_s^2}{2Rc} = \frac{\lambda^2 R}{8\pi^2 c l_{\text{diff}}^2}. \quad (46)$$

Using Eq.(44) and $\Delta R \sim R$, the temporal scattering time satisfies

$$\tau_s(\lambda) \simeq \begin{cases} \frac{3-\beta}{16(2\pi)^{4-\beta}} \frac{f_{1,\alpha} r_e^2}{c l_0} \delta n_e^2 R^2 \lambda^4, & l_{\text{diff}} < l_0, \\ \frac{(3-\beta)^{\frac{2}{\beta-2}}}{2^{\frac{\beta+4}{\beta-2}}} \frac{f_{2,\alpha}^{\frac{2}{\beta-2}} r_e^{\frac{4}{\beta-2}}}{c l_0^{\frac{2(\beta-3)}{\beta-2}}} \delta n_e^{\frac{4}{\beta-2}} R^{\frac{\beta}{\beta-2}} \lambda^{\frac{2\beta}{\beta-2}}, & l_{\text{diff}} > l_0. \end{cases} \quad (47)$$

for $\beta < 3$ and

$$\tau_s(\lambda) \simeq \begin{cases} \frac{\beta-3}{16(2\pi)^{4-\beta}} \frac{f_{1,\alpha} r_e^2 l_0^{\beta-4}}{c L^{\beta-3}} \delta n_e^2 R^2 \lambda^4, & l_{\text{diff}} < l_0, \\ \frac{(\beta-3)^{\frac{2}{\beta-2}}}{2^{\frac{\beta+4}{\beta-2}}} \frac{f_{2,\alpha}^{\frac{2}{\beta-2}} r_e^{\frac{4}{\beta-2}}}{c L^{\frac{2(\beta-3)}{\beta-2}}} \delta n_e^{\frac{4}{\beta-2}} R^{\frac{\beta}{\beta-2}} \lambda^{\frac{2\beta}{\beta-2}}, & l_{\text{diff}} > l_0. \end{cases} \quad (48)$$

for $\beta > 3$. The corresponding scintillation bandwidth is

$$\Delta\nu_{\text{sci}}(\nu) \simeq \frac{1}{2\pi\tau_s} \simeq \begin{cases} \frac{16(2\pi)^{3-\beta}}{3-\beta} \frac{l_0}{c^3 f_{1,\alpha} r_e^2} \delta n_e^{-2} R^{-2} \nu^4, & l_{\text{diff}} < l_0, \\ \frac{2^{\frac{\beta+4}{\beta-2}}}{2\pi(3-\beta)^{\frac{2}{\beta-2}}} \frac{l_0^{\frac{2(\beta-3)}{\beta-2}}}{c^{\frac{\beta+2}{\beta-2}} f_{2,\alpha}^{\frac{2}{\beta-2}} r_e^{\frac{4}{\beta-2}}} \delta n_e^{\frac{4}{2-\beta}} R^{\frac{\beta}{2-\beta}} \nu^{\frac{2\beta}{\beta-2}}, & l_{\text{diff}} > l_0. \end{cases} \quad (49)$$

for $\beta < 3$ and

$$\Delta\nu_{\text{sci}}(\nu) \simeq \frac{1}{2\pi\tau_s} \simeq \begin{cases} \frac{16(2\pi)^{3-\beta}}{\beta-3} \frac{L^{\beta-3}}{c^3 f_{1,\alpha} r_e^2 l_0^{\beta-4}} \delta n_e^{-2} R^{-2} \nu^4, & l_{\text{diff}} < l_0, \\ \frac{2^{\frac{\beta+4}{\beta-2}}}{2\pi(\beta-3)^{\frac{2}{\beta-2}}} \frac{L^{\frac{2(\beta-3)}{\beta-2}}}{c^{\frac{\beta+2}{\beta-2}} f_{2,\alpha}^{\frac{2}{\beta-2}} r_e^{\frac{4}{\beta-2}}} \delta n_e^{\frac{4}{2-\beta}} R^{\frac{\beta}{2-\beta}} \nu^{\frac{2\beta}{\beta-2}}, & l_{\text{diff}} > l_0. \end{cases} \quad (50)$$

for $\beta > 3$. For the Kolmogorov turbulence with $\beta = 11/3$, the typical value of the scintillation bandwidth is given by Eq.(50)

$$\Delta\nu_{\text{sci}} \simeq 130 \text{ MHz } L_{15}^{2/3} l_{0,13}^{1/3} \delta n_{e,3}^{-2} R_{15}^{-2} \nu_9^4, \quad (51)$$

where $l_{\text{diff}} < l_0$ is satisfied for the typical parameters. Therefore, if the spectral shape with a typical bandwidth of $\Delta\nu_{\text{sci}} \sim 100$ MHz is attributed to the plasma screen, the environment near the FRB source would be required to be intermediately dense (e.g. $n_e \sim \delta n_e \sim 10^3 \text{ cm}^{-3}$ at $R \sim 10^{15} \text{ cm}$) and turbulent.

6.2. Gravitational lensing

The time-delay effect of gravitational lensing can modulate the spectrum of a transient (Gould 1992; Barnacka et al. 2012), which mainly depends on the mass and position of the lensing object. We consider the lensing object has a mass of M . The distances from the lens to the FRB source, from the observer to the lens, and from the observer to the FRB source are d_{ls} , d_{ol} and d_{os} , respectively. The Einstein radius of gravitational lensing is

$$r_{\text{E}} = \left(\frac{4GM}{c^2} \frac{d_{\text{ol}} d_{\text{ls}}}{d_{\text{os}}} \right)^{1/2}. \quad (52)$$

We define the source position projected onto the lens plane as r_{s} , then the image positions are given by

$$r_{\pm} = \frac{1}{2} \left(r_{\text{s}} \pm \sqrt{r_{\text{s}}^2 + 4r_{\text{E}}^2} \right). \quad (53)$$

The time delay between the two images is

$$\delta t = \frac{2GM}{c^3} \left[\left(\frac{r_{+}}{r_{\text{E}}} \right)^2 - \left(\frac{r_{-}}{r_{\text{E}}} \right)^2 + 2 \ln \left| \frac{r_{+}}{r_{-}} \right| \right]. \quad (54)$$

The phase difference between the rays from the two images is

$$\delta\phi = 2\pi\nu\delta t. \quad (55)$$

A gravitational lensing event with remarkable spectral modulation requires $\delta\phi \sim 1$ and $r_{\text{s}} \lesssim r_{\text{E}}$, leading to

$$\delta t = \frac{1}{2\pi\nu} \simeq 1.6 \times 10^{-10} \text{ s } \nu_9^{-1}, \quad (56)$$

$$M \sim \frac{c^3 \delta t}{G} \simeq 2.0 \times 10^{-5} M_{\odot} \delta t_{-10}. \quad (57)$$

The time delay between two images is much shorter than the durations of FRBs, and the lens is required to be the planet-like object. The amplitude contributed by the image at position r_{\pm} is $\mathcal{A}_{\pm} \propto \exp(i\phi) / \sqrt{|1 - r_{\text{E}}^4/r_{\pm}^4|}$

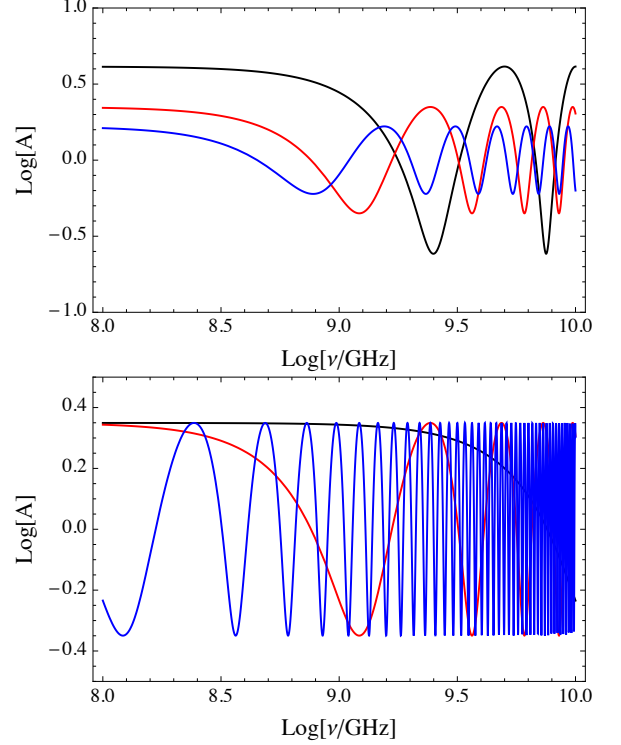


Figure 9. The amplification of the gravitational lensing as a function of frequency. The top panel takes the lens mass as $M = 10^{-5} M_{\odot}$. The black, red, and blue lines correspond to $r_{\text{s}}/r_{\text{E}} = 0.5, 1.0, 1.5$, respectively. The bottom panel takes the source projected position as $r_{\text{s}}/r_{\text{E}} = 1.0$. The black, red, and blue lines correspond to the lens mass of $M = 10^{-6} M_{\odot}, 10^{-5} M_{\odot}, 10^{-4} M_{\odot}$, respectively. The distances from the lens to the FRB source, from the observer to the lens, and from the observer to the FRB source are taken as $d_{\text{ls}} = 1 \text{ kpc}$, $d_{\text{ol}} = 1 \text{ Gpc}$ and $d_{\text{os}} = 1 \text{ Gpc}$, respectively.

(e.g., Barnacka et al. 2012). The amplification is obtained by summing the amplitudes of the two images, $A \equiv |\mathcal{A}|^2 = |\mathcal{A}_{+} + \mathcal{A}_{-}|^2$, which is given by

$$A = \frac{1}{|1 - r_{\text{E}}^4/r_{+}^4|} + \frac{1}{|1 - r_{\text{E}}^4/r_{-}^4|} + \frac{2 \cos \delta\phi}{\sqrt{|1 - r_{\text{E}}^4/r_{+}^4|} \sqrt{|1 - r_{\text{E}}^4/r_{-}^4|}}. \quad (58)$$

In Figure 9, we plot the amplification A of the gravitational lensing as a function of frequency. We take the distances as $d_{\text{ls}} = 1 \text{ kpc}$, $d_{\text{ol}} = 1 \text{ Gpc}$ and $d_{\text{os}} = 1 \text{ Gpc}$, respectively. The top panel takes the lens mass as $M = 10^{-5} M_{\odot}$, and the black, red, and blue lines correspond to $r_{\text{s}}/r_{\text{E}} = 0.5, 1, 1.5$, respectively. The bottom panel takes the source projected position as $r_{\text{s}}/r_{\text{E}} = 1.0$. The black, red, and blue lines correspond to the lens mass of $M = 10^{-6} M_{\odot}, 10^{-5} M_{\odot}, 10^{-4} M_{\odot}$, respectively. We can see that spectral modulation becomes significant

at GHz band only when $M \sim 10^{-5} M_\odot$ and $r_s \sim r_E$ as pointed out above.

Although a planet-like object can generate the spectral modulation at the GHz band, the observed variation of the spectra of an FRB repeater seems not to support such a scenario due to the following reasons. For the above distance parameters, the typical lensing timescale is

$$t_{\text{lens}} = \frac{r_E}{v} \sim 10^4 \text{ s } M_{\odot,-5} v_7^{-1} d_{\text{os,Gpc}}^{-1/2} d_{\text{ol,Gpc}}^{1/2} d_{\text{ls,kpc}}^{1/2}, \quad (59)$$

where v is the transverse velocity of the lens. This timescale is much shorter than the several-year active period of an FRB repeater. The observation of FRB repeaters showed that the burst-to-burst spectral variation is always present during the active periods. If the variation is due to the gravitational lensing, one would not see the persistent variation of the spectra during the long term, because the gravitational lensing event is most likely one-time. On the other hand, this timescale is much longer than the waiting time of an FRB repeater with a significant variation of spectra. It cannot explain the remarkable burst-to-burst variation of the spectra in an extremely short time, e.g., the spectrum variation of two components in FRB 200428 (CHIME/FRB Collaboration et al. 2020). Therefore, the spectral modulation by gravitational lensing could be ruled out.

6.3. Plasma lensing

Plasma lensing plays an important role in the “extreme scattering events” as shown in the light curves of some radio pulsars and active galactic nuclei (Fiedler et al. 1987; Bannister et al. 2016). Similar to gravitational lensing discussed in Section 6.2, plasma lensing can also cause the time-delay effect. However, the time delay in plasma lensing is frequency-dependent due to the plasma dispersion (e.g., Er et al. 2020), which would lead to a different spectral modulation compared to that of gravitational lensing.

Following Cordes et al. (2017), we consider the plasma structure has a form with the dispersion measure satisfying $\text{DM}(x) = \text{DM}_l \exp(-x^2/a^2)$, which yields a phase perturbation $\phi_\lambda = -\lambda r_e \text{DM}(x)$, where λ is the wavelength and r_e is the classical electron radius. The distances from the lens to the FRB source, from the observer to the lens, and from the observer to the FRB source are d_{ls} , d_{ol} and d_{os} , respectively. The transverse coordinates in the source, lens, and observer’s planes are x_s , x and x_o , and one defines the dimensionless coordinates $u_s = x_s/a$, $u = x/a$ and $u_o = x_o/a$, respectively. The effective transverse offset can be expressed as $u' = (d_{\text{ol}}/d_{\text{os}})u_s + (d_{\text{ls}}/d_{\text{os}})u_o$. The lens equation in geometric optics gives (Clegg et al. 1998; Cordes et al.

2017)

$$u[1 + \alpha \exp(-u^2)] = u', \quad (60)$$

where the parameter α is given by

$$\alpha = \frac{\lambda^2 r_e \text{DM}_l}{\pi a^2} \left(\frac{d_{\text{ol}} d_{\text{ls}}}{d_{\text{os}}} \right). \quad (61)$$

There are either one or three solutions for u for a given offset u' based on Eq.(60) (see the detailed discussion in Cordes et al. 2017). Due to the limited spatial resolution of radio telescopes, the separated images might be extremely difficult to resolve. In the geometrical optics regime, the focusing or defocusing of incident wavefronts yields an amplification (Clegg et al. 1998; Cordes et al. 2017)

$$A = |1 + \alpha(1 - 2u^2) \exp(-u^2)|^{-1}. \quad (62)$$

At $\alpha = \alpha_{\text{min}} = e^{3/2}/2$ and $|u| = \sqrt{3/2}$, the amplification reaches $A \rightarrow \infty$ (Cordes et al. 2017). The actual physical optics gains should be finite, and the maximum value is

$$A_{\text{max}} \sim \frac{a}{r_F} = a \sqrt{\frac{2\pi d_{\text{os}}}{\lambda d_{\text{ol}} d_{\text{ls}}}} \simeq 3.9 \nu_9^{1/2} a_{\text{AU,-3}} d_{\text{os,Gpc}}^{1/2} d_{\text{ol,Gpc}}^{-1/2} d_{\text{ls,pc}}^{-1/2}, \quad (63)$$

where $r_F = \sqrt{\lambda d_{\text{ol}} d_{\text{ls}} / 2\pi d_{\text{os}}}$ is the Fresnel scale, $a_{\text{AU,-3}} = a/10^{-3} \text{AU}$, $d_{\text{os,Gpc}} = d_{\text{os}}/\text{Gpc}$, $d_{\text{ol,Gpc}} = d_{\text{ol}}/\text{Gpc}$, and $d_{\text{ls,pc}} = d_{\text{ls}}/\text{pc}$. The focal frequency is defined as

$$\nu_f = \nu \left(\frac{\alpha}{\alpha_{\text{min}}} \right)^{1/2} = \frac{c}{a} \left(\frac{r_e \text{DM}_l}{\pi \alpha_{\text{min}}} \frac{d_{\text{ol}} d_{\text{ls}}}{d_{\text{os}}} \right)^{1/2} \simeq 0.12 \text{ GHz } \text{DM}_{l,-8}^{1/2} a_{\text{AU,-3}}^{-1} d_{\text{os,Gpc}}^{-1/2} d_{\text{ol,Gpc}}^{1/2} d_{\text{ls,pc}}^{1/2}, \quad (64)$$

where $\text{DM}_{l,-8} = \text{DM}_l / (10^{-8} \text{ pc cm}^{-3})$. The frequency below ν_f will show ray crossings (Cordes et al. 2017).

According to Eq.(60) and Eq.(62), one can obtain the amplification as a function of the dimensionless frequency ν/ν_f , as shown in Figure 5 of Cordes et al. (2017). There are two caustic peaks in the amplified spectra with widths of (1–10)% of the observation frequency ν , which are contributed by individual subimages by the Gaussian plasma lensing. The amplification is suppressed below the unit at the frequency $\nu \ll \nu_f$ and asymptotes to the unity at $\nu \gg \nu_f$ due to the caustic.

Similar to the scenario of gravitational lensing discussed in Section 6.2, if the time delays of subimaged bursts are smaller than their durations, the total image would be interfered, leading to the oscillating structures on the spectra. Due to the plasma dispersion along the

line of sight, the arrival times of subimages should be chromatic, here we are only interested in the perturbations from the plasma lens, which add to delays from other plasma components (e.g., interstellar medium, intergalactic medium, etc.). The typical delay timescale of the plasma lensing is about (Cordes et al. 2017)

$$\delta t \sim \frac{cr_e DM_l}{2\pi\nu^2} \simeq 4.1 \times 10^{-11} \text{ s } DM_{l,-8\nu_9}^{-2}. \quad (65)$$

The phase difference of the rays from the two images is $\delta\phi = 2\pi\nu\delta t$. A plasma lensing event with remarkable spectral modulation requires $\delta\phi \sim 1$, $\nu \sim \nu_f$ and $A_{\max} > 1$, leading to

$$DM_l \sim \frac{\nu}{cr_e} \simeq 3.8 \times 10^{-8} \text{ pc cm}^{-3} \nu_9, \quad (66)$$

$$a_{\text{AU},-3}^{-1} d_{\text{ls,pc}}^{1/2} \sim 4.1. \quad (67)$$

Therefore, a remarkable spectral modulation requires that the lensing object has an average electron number density of $n_e \sim 10 \text{ cm}^{-3}$ and a typical scale of $a \sim 10^{-3} \text{ AU}$ at a distance of $d_{\text{ls}} \sim 1 \text{ pc}$ from the FRB source.

The variation timescale of the spectra depends on the changes in amplification through caustics due to the motions of source and observer. The effective transverse velocity combined into the motions of the source and the observer is $v_{\perp} = (d_{\text{ol}}/d_{\text{os}})v_{s,\perp} + (d_{\text{ls}}/d_{\text{os}})v_{o,\perp}$. Using Eq.(60) and Eq.(62) and taking the derivatives, one has $\delta u' \sim (\delta A/A)A^2$ for $u \sim 1$ when the amplification reaches the maximum value. Using $\delta u' \sim v_{\perp} t_{\text{cau}}/a$, the timescale of a caustic crossing (also the variation timescale of the spectra) is estimated as

$$t_{\text{cau}} \sim \frac{a(\delta A/A)}{v_{\perp} A^2} \simeq 15 \text{ s } a_{\text{AU},-3} v_{\perp,7}^{-1} A_1^{-2} (\delta A/A). \quad (68)$$

Therefore, a plasma lensing can cause the burst-to-burst variation of the spectra during a much shorter time compared with that of the gravitational lensing. The variation timescale of the spectra of the two components of FRB 200428 might a relatively extreme amplification of $A \sim 100$.

7. DISCUSSIONS AND CONCLUSIONS

Some FRBs appear significantly intrinsic narrow spectra in the telescope's bandwidth (Pleunis et al. 2021; Kumar et al. 2021; Zhou et al. 2022), which is an important clue to reveal the radiation mechanism and the environment of FRBs. In this work, we investigated the physical origin of the narrow spectra of FRBs from the perspectives of radiation mechanisms, coherent processes, radiative transfers, and interference processes, and the following conclusions are drawn:

1. Without considering the finite bandwidth of a telescope, the relative spectral bandwidth defined by FWHM or FWTM only depends on the intrinsic spectral shape. Some FRBs (e.g., FRB 20190711A, Kumar et al. (2021)) showed that their spectra must be intrinsically narrow $\Delta\nu/\nu_0 \ll 0.2$ for FWHM. This gives a strong constraint on the radiation mechanisms of FRBs because most radiation mechanisms with low-frequency spectral index $\alpha_l < 3$ lead to wide spectra with $\Delta\nu/\nu_0 > 0.2$ for FWHM. In reality, the narrow telescope's bandwidth usually makes some observed bursts' spectra incomplete, and the distribution of the observed relative spectral bandwidths would be affected by the limited telescope's bandwidth.

2. An intrinsic narrow spectrum with $\Delta\omega/\omega_0 \ll 1$ (ω_0 is the peak frequency and $\Delta\omega$ is the spectral bandwidth) implies that the electromagnetic wave is quasi-sinusoid with a typical frequency of $\omega \sim \omega_0$ in a short term and have a typical pulse duration of $T \sim 4\pi/\Delta\omega$ in a long term. We generally discuss the spectral shapes and polarization distributions from the perspective of radiation mechanisms. For the radiation mechanisms involving the relativistic particle's perpendicular acceleration, the radiation features (including the spectrum and polarization) depend on the relation between the particle's deflection angle ψ and the radiation beaming angle $1/\gamma$. The scenarios with $\gamma\psi \gg 1$ and $\gamma\psi \ll 1$ lead to different features of the spectrum and polarization.

3. For the scenario of $\gamma\psi \gg 1$, the observer would see radiation from short segments of the particle's trajectory that are nearly parallel to the line of sight. Such a scenario is applicable to the curvature radiation and the traditional (large-pitch-angle) synchrotron radiation. The intrinsic spectra of these mechanisms are usually wide, and the intrinsic linear/circular polarization degree mainly depends on the angle between the viewing direction and the trajectory plane. If $\gamma\psi \ll 1$, the particle's entire trajectory would be seen by the observer during a long term. In particular, for the small-pitch-angle synchrotron radiation by a single charged particle, the radiation is only emitted at a certain frequency within an extremely narrow band for a certain viewing direction, and the circular polarization is dominated. Furthermore, we discussed some astrophysical scenarios that might involve radiation processes with $\gamma\psi \gg 1$ and $\gamma\psi \ll 1$. In the magnetosphere of a neutron star, the radiation process with $\gamma\psi \gg 1$ occurs in the inner magnetosphere and the corresponding radiation mechanism is the curvature radiation and the radiation process with $\gamma\psi \ll 1$ occurs in the outer magnetosphere and the corresponding radiation mechanism is the small-pitch-angle synchrotron radiation. On the other hand,

both scenarios with $\gamma\psi \gg 1$ and $\gamma\psi \ll 1$ might occur in the magnetized shocked medium, which corresponds to the traditional synchrotron radiation and the small-pitch-angle radiation, respectively. However, the generation of the small-pitch-angle radiation requires that the direction of the particles' injection is almost parallel to the field lines, which seems fine-tuning.

4. We find that coherent radiation processes can generate narrow spectra. For the bunching mechanisms (e.g., coherent curvature radiation), one possibility to generate a narrow spectrum is that the radiating bunches are quasi-periodically distributed. The quasi-periodic distribution of bunches might be due to the quasi-monochromatic Langmuir waves or quasi-periodic oscillating pair creation in the charge-starved region. For a train of bunches separated by a period of $1/\omega_m$, the total radiation will be coherently amplified at the peak frequencies of $\omega = 2n\pi\omega_m$ with $n \in \mathbb{Z}^+$ that is independent of the radiation mechanism of the bunches. In particular, we notice that the bunches are not required to be positioned at exactly the same distance from each other. A small random relative phase of $\delta\phi_j \ll \pi$ can still lead to the coherent amplification at $\omega = 2n\pi\omega_m$. However, once $\delta\phi_j \sim \pi$, the total radiation would become completely incoherent. On the other hand, the maser mechanism can naturally arise a narrow spectrum because a negative optical depth of τ_ν causes an amplification by a factor of $\exp(|\tau_\nu|)$. An intermediate negative optical depth naturally causes the spectrum narrow.

5. The radiative transfer processes mainly include absorption and scattering. Based on the current observation, most processes seem not to significantly change the observed FRB spectra or directly arise a narrow spectral shape. The absorption processes can cause the radio bursts emitted during a short term to have the same low-frequency cutoff at the absorption frequency, which is inconsistent with the observations of some FRBs, e.g., the burst-to-burst spectral variation of two components of FRB 200428. Inverse Compton scattering suppresses the specific intensity in all bands but can not change the spectral shape. Induced Compton scattering redistributes the incident photons toward low frequencies, and the photons are eventually absorbed by the absorption processes, leading to the same issue as the absorption. The nonlinear scattering depends on the radiation intensity and frequency and makes the low-frequency cutoff proportional to the intensity, which is worthy to test the nonlinear effect by the observations of FRB repeaters.

6. We discussed some interference processes including scintillation, gravitational lensing, and plasma lensing. If the scintillation significantly changes the observed shape, the scintillation bandwidth is required to be $\Delta\nu_{\text{sci}} \gtrsim 100$ MHz, which is much larger than the observed narrow-bandwidth scintillation with $\Delta\nu_{\text{sci}} \sim 1$ MHz. Thus, involving another plasma screen is necessary to modulate the spectra at a bandwidth of $\gtrsim 100$ MHz. The scintillation with $\Delta\nu_{\text{sci}} \gtrsim 100$ MHz requires that the corresponding plasma screen is within a distance of $\sim 10^{15}$ cm from the FRB source and the plasma medium is intermediately dense and turbulent. The spectral modulations of gravitational lensing and plasma lensing can modulate the FRB spectra when the time delay of subimaged bursts is about $\delta t \sim 10^{-10}$ s for GHz wave. For gravitational lensing, such a condition requires that the lensing object has a mass of $\sim 10^{-5}M_\odot$, i.e., a planet-like object. However, since the gravitational lensing event is most likely one-time but the spectrum variation is always present during the several-year active period of an FRB repeater, such a scenario could be ruled out. Besides, the gravitational lensing cannot explain the remarkable burst-to-burst variation of the spectra in a time shorter than the typical lensing timescale. The delay time of $\delta t \sim 10^{-10}$ s requires the plasma lens has an average electron number density of $n_e \sim 10$ cm $^{-3}$ and a typical scale of $a \sim 10^{-3}$ AU at a distance of $d_{\text{ls}} \sim 1$ pc from the FRB source. These conditions are moderate to explain the observed FRB spectra. Meanwhile, the typical lensing time scale of decades of seconds can cause the spectrum variation during a short time, although the extremely short spectrum variation as shown in FRB 200428 might be due to a relatively extreme amplification.

ACKNOWLEDGMENTS

We thank the anonymous referee for the helpful comments and suggestions. We also thank Bing Zhang and Yue Wu for reading the initial manuscript and for their helpful comments and acknowledge the discussions with Yi Feng, Jin-Lin Han, Kejia Lee, Ze-Nan Liu, Yuanhong Qu, Wei-Yang Wang, and Yong-Kun Zhang. This work is supported by the National Natural Science Foundation of China grant No.12003028 and the National SKA Program of China (2022SKA0130100).

APPENDIX

A. RADIATIONS BY A SINGLE CHARGED PARTICLES

In this appendix, we generally discuss the features of the spectra and polarizations of the radiation by charged accelerated particles, which are applicable to most radiation mechanisms in various astrophysical scenarios. We consider that a particle with a charge q moves on a trajectory $\vec{r}_0(t')$ with velocity $\vec{\beta}(t')c$ and acceleration $\dot{\vec{\beta}}(t')c$, where t' is the retarded time. The line-of-sight direction is \vec{n} and the distance between the particle and the observer is R . The radiation field at (\vec{r}, t) is given by (e.g., Rybicki & Lightman 1986)

$$\begin{aligned}\vec{E}(\vec{r}, t) &= \frac{q}{c} \left[\frac{\vec{n}}{\kappa^3 R} \times \{(\vec{n} - \vec{\beta}) \times \dot{\vec{\beta}}\} \right]_{\text{rec}}, \\ \vec{B}(\vec{r}, t) &= [\vec{n} \times \vec{E}]_{\text{rec}},\end{aligned}\quad (\text{A1})$$

where $\kappa \equiv 1 - \vec{n} \cdot \vec{\beta}$, the quantities in the square bracket, $[\dots]_{\text{rec}}$, are evaluated at the retarded time t' . The radiation energy per unit frequency interval per unit solid angle is

$$\mathcal{E}_\omega \equiv \frac{dW}{d\omega d\Omega} = \frac{q^2}{4\pi^2 c} \left| \int_{-\infty}^{\infty} \left[\kappa^{-3} \vec{n} \times \{(\vec{n} - \vec{\beta}) \times \dot{\vec{\beta}}\} \right]_{\text{rec}} e^{i\omega t} dt \right|^2 \quad (\text{A2})$$

$$= \frac{q^2 \omega^2}{4\pi^2 c} \left| \int \vec{n} \times (\vec{n} \times \vec{\beta}) \exp[i\omega(t' - \vec{n} \cdot \vec{r}_0(t')/c)] dt' \right|^2 \quad (\text{A3})$$

$$= \frac{e^2 \omega^2}{4\pi^2 c} |-\epsilon_{\parallel} A_{\parallel}(\omega) + \epsilon_{\perp} A_{\perp}(\omega)|^2, \quad (\text{A4})$$

where A_{\parallel} and A_{\perp} are two orthogonal components perpendicular to the line of sight. The linear polarization degree is

$$\pi_L = \left| \frac{[(A_{\parallel} A_{\parallel}^* - A_{\perp} A_{\perp}^*)^2 + (A_{\parallel} A_{\perp}^* + A_{\perp} A_{\parallel}^*)^2]^{1/2}}{A_{\parallel} A_{\parallel}^* + A_{\perp} A_{\perp}^*} \right|, \quad (\text{A5})$$

and the circular polarization degree is

$$\pi_V = \left| \frac{1}{i} \frac{A_{\parallel} A_{\perp}^* - A_{\perp} A_{\parallel}^*}{A_{\parallel} A_{\parallel}^* + A_{\perp} A_{\perp}^*} \right|. \quad (\text{A6})$$

It should be noted that the \mathcal{E}_ω corresponds to the total radiation energy in an entire pulse. If the radiation pulse repeats on average time T , the above radiation energy could be converted to the radiation power (Rybicki & Lightman 1986)

$$\mathcal{P}_\omega \equiv \frac{1}{T} \frac{dW}{d\omega d\Omega} = \frac{\mathcal{E}_\omega}{T}. \quad (\text{A7})$$

The radiation spectrum by a single charged particle with the perpendicular acceleration depends on the relation between the particle's deflection angle ψ and the radiation beaming angle $\sim 1/\gamma$ (Landau & Lifshitz 1975), as shown in Figure 4, which will be summarized in the following subsections.

A.1. Deflection angle larger than radiation beaming angle

In the scenario with $\gamma\psi \gg 1$, the radiation is equivalent to the radiation by the particle moving instantaneously at constant speed on an appropriate circular path (Jackson 1998), as shown in the panel (a) of Figure 4. We consider that the acceleration curvature radius is ρ , the angle between the line of sight and the trajectory plane is θ , and the radiation angular frequency is ω . The radiation energy per unit frequency interval per unit solid angle is given by the above equation with (Jackson 1998)

$$A_{\parallel}(\omega) = \frac{2i}{\sqrt{3}} \frac{\rho}{c} \left(\frac{1}{\gamma^2} + \theta^2 \right) K_{2/3}(\xi), \quad (\text{A8})$$

$$A_{\perp}(\omega) = \frac{2}{\sqrt{3}} \frac{\rho\theta}{c} \left(\frac{1}{\gamma^2} + \theta^2 \right)^{1/2} K_{1/3}(\xi), \quad (\text{A9})$$

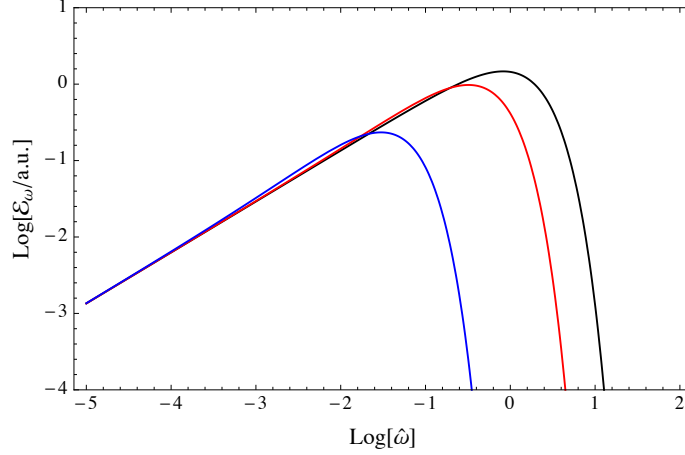


Figure 10. The spectrum given by Eq.(12) that is applicable for the scenario with the particle’s deflection angle larger than the radiation beaming angle, $\gamma\psi \gg 1$. The black, red, and blue lines correspond to $\gamma\theta = 0.1, 1$ and 3 , respectively. The unit of \mathcal{E}_ω is arbitrary.

and

$$\xi \equiv \frac{1}{2}\hat{\omega} (1 + \gamma^2\theta^2)^{3/2} \quad \text{with} \quad \hat{\omega} \equiv \frac{\omega}{\omega_c}, \quad (\text{A10})$$

where $\omega_c = 3\gamma^3 c/2\rho$ is the typical radiation frequency. The radiation energy per unit frequency interval per unit solid angle is

$$\mathcal{E}_\omega = \frac{3e^2}{4\pi^2 c} \gamma^2 \hat{\omega}^2 (1 + \gamma^2\theta^2)^2 \left[K_{2/3}^2(\xi) + \frac{1}{1/\gamma^2\theta^2 + 1} K_{1/3}^2(\xi) \right]. \quad (\text{A11})$$

The spectrum \mathcal{E}_ω of a single radiating particle satisfies the power-law distribution with $\mathcal{E}_\omega \propto \hat{\omega}^{2/3}$ at the low frequency and appears an exponential decay at the high frequency, which is intrinsically wide (e.g., Jackson 1998; Yang & Zhang 2018a), $\Delta\omega/\omega_0 \sim 1$ (see Section 2.1), as shown in Figure 10. Meanwhile, the larger the viewing angle $\gamma\theta$, the lower the cutoff frequency. The spectrum of the radiation by multiple particles is also usually wide, which has been discussed in detail in (Yang & Zhang 2018a, 2023) and we will not repeat it here. According to Eq.(A5), Eq.(A6), Eq.(A8) and Eq.(A9), the linear polarization degree is

$$\pi_L = \left| \frac{K_{2/3}^2(\xi) - 1/(1/\gamma^2\theta^2 + 1)K_{1/3}^2(\xi)}{K_{2/3}^2(\xi) + 1/(1/\gamma^2\theta^2 + 1)K_{1/3}^2(\xi)} \right|, \quad (\text{A12})$$

and the circular polarization degree is

$$\pi_V = \left| \frac{2/(1/\gamma^2\theta^2 + 1)^{1/2} K_{2/3}(\xi) K_{1/3}(\xi)}{K_{2/3}^2(\xi) + 1/(1/\gamma^2\theta^2 + 1)K_{1/3}^2(\xi)} \right|. \quad (\text{A13})$$

Similar to the spectrum given by \mathcal{E}_ω , both π_L and π_V are also the functions as the variables $(\hat{\omega}, \gamma\theta)$. In Figure 11, we plot the linear and circular polarization degrees Π_i with $i = L$ and V as the functions of the dimensionless frequency $\hat{\omega}$ and the viewing angle $\gamma\theta$, respectively. For a certain viewing angle $\gamma\theta$, the higher the frequency $\hat{\omega}$, the lower (higher) the linear (circular) polarization degree. For a certain frequency $\hat{\omega}$, the larger the viewing angle $\gamma\theta$, the lower (higher) the linear (circular) polarization degree. Thus, the high circular polarization degree should be attributed to the off-beam observation (Wang et al. 2022a; Liu et al. 2023; Qu & Zhang 2023).

The polarization measurement at least requires that burst flux larger than the telescope’s threshold. For the scenario with $\gamma\psi \gg 1$, according to Eq.(12) and using the property of Bessel function, $K_\nu(x) \sim \sqrt{\pi/2x} \exp(-x)$ for $x \gg 1$, the radiation energy falls off in angle approximately as

$$\mathcal{E}_\omega \sim \mathcal{E}_{\omega,0} \exp(-\hat{\omega}\gamma^3\theta^3), \quad (\text{A14})$$

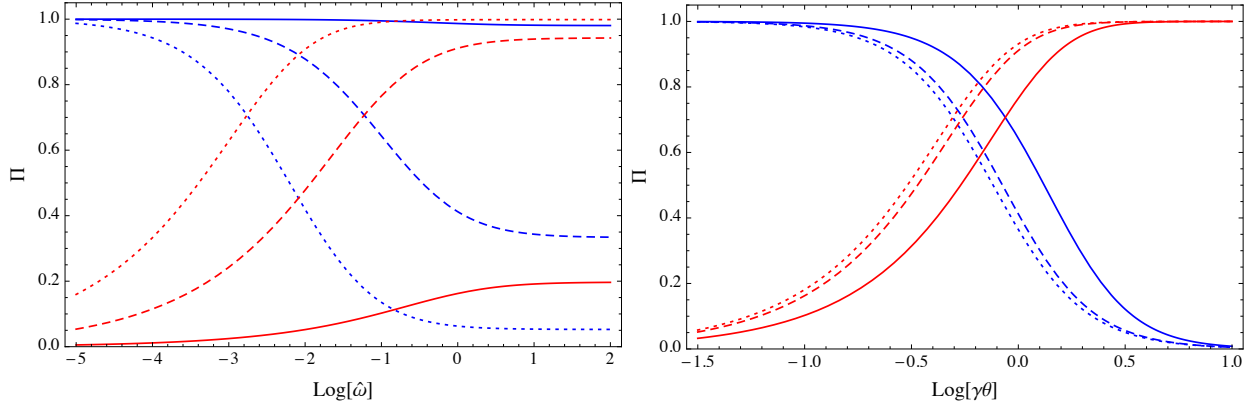


Figure 11. The relations between the polarization degree Π and the dimensionless frequency $\hat{\omega}$ and the viewing angle $\gamma\theta$ for a single radiating particle with $\gamma\psi \gg 1$. The blue and red lines correspond to the linear and circular polarization degrees, respectively. The top panel shows the polarization degree Π as the function of the dimensionless frequency $\hat{\omega}$. The solid, dashed, and dotted lines correspond to $\gamma\theta = 0.1, 1$ and 3 , respectively. The bottom panel shows the polarization degree Π as the function of the viewing angle $\gamma\theta$. The solid, dashed, and dotted lines correspond to $\hat{\omega} = 0.1, 1$ and 3 , respectively.

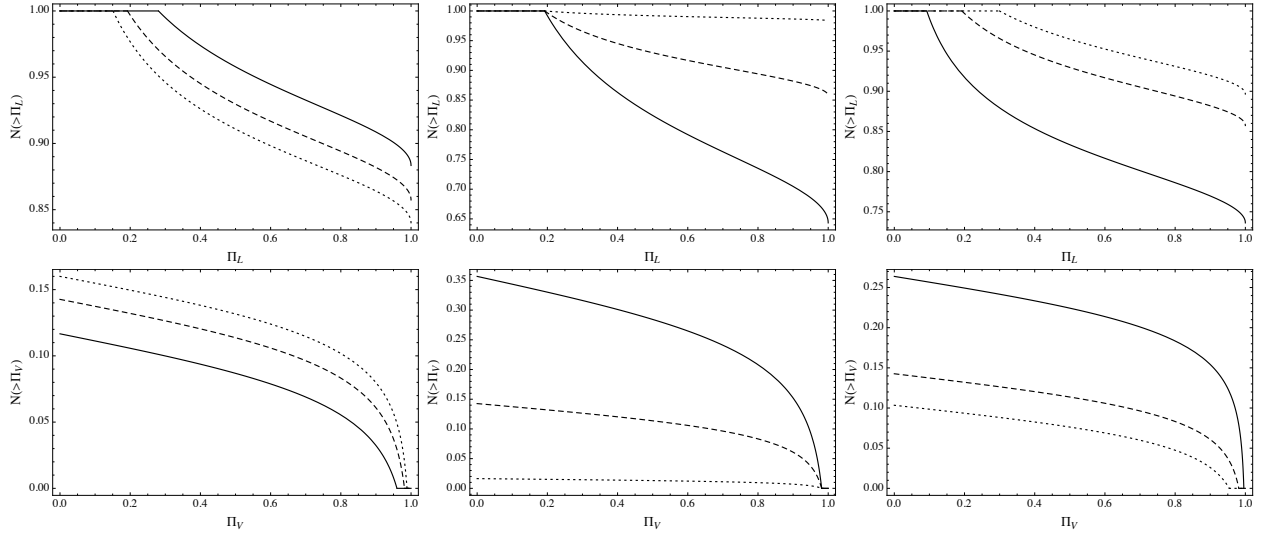


Figure 12. The cumulative distribution of the linear (top panels) and circular (bottom panels) polarization degrees for the radiation by multiple particles with $\gamma\psi \gg 1$. Notice that the cumulative distribution of the circular polarization degrees is $N(> \Pi_V = 0) = 1$ at $\Pi_V = 0$ and decreases significantly once $\Pi_V > 0$. The component of $N(> \Pi_V = 0) = 1$ at $\Pi_V = 0$ is not shown in the bottom panels. The distribution function of the viewing direction is assumed to satisfy Eq.(A19). In the left panels: the solid, dashed, and dotted lines correspond to $\eta_c = 10, 100$ and 1000 , respectively for $\hat{\omega} = 1$ and $\gamma\Theta_j = 10$. In the middle panels: the solid, dashed, and dotted lines correspond to $\gamma\Theta_j = 3, 10$ and 100 , respectively for $\hat{\omega} = 1$ and $\eta_c = 100$. In the right panels: the solid, dashed, and dotted lines correspond to $\hat{\omega} = 0.1, 1$ and 3 , respectively for $\gamma\Theta_j = 10$ and $\eta_c = 100$.

where $\mathcal{E}_{\omega,0} \equiv \mathcal{E}_{\omega}(\theta = 0)$ and $\mathcal{E}_{\omega} \propto K_{\nu}^2(\xi)$ is used. We consider that only the burst with radiation energy

$$\mathcal{E}_{\omega} > \eta_c^{-1} \mathcal{E}_{\omega,0} \quad \text{with } \eta_c \geq 1 \quad (\text{A15})$$

could be observed due to the constraint of a detector's sensitivity, leading to

$$\gamma\theta < \gamma\theta_{\text{th}} \equiv \left(\frac{1}{\hat{\omega}} \ln \eta_c \right)^{1/3}. \quad (\text{A16})$$

Only the bursts with viewing angle $\theta < \theta_{\text{th}}$ are observable. Notice that the distribution of the intrinsic burst energies is neglected, and here we are mainly interested in the suppression effect by the viewing direction.

We consider that multiple radiating particles are uniformly distributed in a fan beam with an opening angle Θ_j , and the viewing angle is Θ . According to Eq.(A12) and Eq.(A13), the polarization is 100% linear when the viewing direction is on the trajectory plane, and most radiation energy is emitted near the trajectory plane. The larger the viewing angle, the higher the circular polarization degree. Since the circular polarizations on the different sides of the trajectory plane are opposite, in the particles' beam center the coherent sum of the circular polarizations will be canceled, leading to the linear polarization dominated. A detailed analysis was also discussed in Wang et al. (2022b) and Liu et al. (2023). Therefore, the linear polarization degree could be approximately given by

$$\Pi_L \simeq \begin{cases} 1, & \text{for } \Theta \leq \Theta_j, \\ \pi_L(\Theta - \Theta_j), & \text{for } \Theta > \Theta_j, \end{cases} \quad (\text{A17})$$

and the circular polarization degree could be approximately given by

$$\Pi_V \simeq \begin{cases} 0, & \text{for } \Theta \leq \Theta_j, \\ \pi_V(\Theta - \Theta_j), & \text{for } \Theta > \Theta_j, \end{cases} \quad (\text{A18})$$

Since the view direction related to the trajectory plane is random, the number of the bursts emitting within $(\Theta, \Theta + d\Theta)$ is ⁸

$$N(\Theta)d\Theta = \frac{1}{(\Theta_j + \theta_{\text{th}})} d\Theta, \quad (\text{A19})$$

where θ_{th} is given by Eq.(A16), and $\Theta_j + \theta_{\text{th}}$ corresponds to the threshold angle above which the observed flux would be less than the telescope's flux threshold. Therefore, the cumulative distribution of the linear and circular polarization degrees are

$$N(> \Pi_L) = \frac{\gamma\Theta_j + (\gamma\theta)(\Pi_L)}{\gamma\Theta_j + \gamma\theta_{\text{th}}}, \quad (\text{A20})$$

$$N(> \Pi_V) = \frac{\gamma\theta_{\text{th}} - (\gamma\theta)(\Pi_V)}{(\gamma\Theta_j + \gamma\theta_{\text{th}})}, \quad (\text{A21})$$

for $(\gamma\theta)(\Pi_i) \leq \gamma\theta_{\text{th}}$ with $i = L, V$, respectively, where $(\gamma\theta)(\Pi_i)$ is the inverse function of $\pi_i(\gamma\theta)$ given by Eq.(A12) and Eq.(A13).

In Figure 12, we plot the cumulative distributions of the linear and circular polarization degrees according to Eq.(A20) and Eq.(A21). The cumulative distributions of the polarization degrees depend on the telescope's flux threshold η_c , the particles' beaming angle $\gamma\Theta_j$, and observed frequency $\hat{\omega}$. We can see that: (1) The higher the telescope's sensitivity (i.e., a large value of η_c), the lower the number fraction between the linearly and circularly polarized bursts. The reason is that most high circularly polarized bursts have relatively low fluxes due to large values of $\gamma\theta$. (2) The larger the particles' beaming angle, the higher the number fraction between the linearly and circularly polarized bursts. If $\gamma\Theta_j \gg 1$, most bursts would have $\Pi_L \sim 1$ and $\Pi_V \sim 0$. A moderate number fraction between linearly polarized bursts and circularly polarized bursts as shown in FRB 20201124A (Xu et al. 2022; Jiang et al. 2022) requires that $\gamma\Theta_j \sim 1$. (3) The higher the observed frequency, the higher the number fraction between the linearly and circularly polarized bursts. The reason is that the threshold viewing angle $\gamma\theta_{\text{th}}$ is significantly suppressed at the high frequency (see Eq.(A16)), leading to a larger relative number of the bursts from the particle beaming angle Θ_j .

A.2. Deflection angle smaller than radiation beaming angle

In the scenario with $\gamma\psi \ll 1$, the particle with a charge q moves along the line of sight with an almost constant velocity $\vec{\beta}$ but with a varying acceleration $\dot{\vec{\beta}}$, as shown in the panel (b) of Figure 4. The radiation energy per unit frequency interval per unit solid angle at the line-of-sight direction \vec{n} could be written as (Landau & Lifshitz 1975, also see Appendix A)

$$\mathcal{E}_\omega = \frac{q^2}{4\pi^2 c} \left(\frac{\omega}{\bar{\omega}}\right)^4 \left| \vec{n} \times \left[(\vec{n} - \vec{\beta}) \times \dot{\vec{\beta}}_{\bar{\omega}} \right] \right|^2 \quad (\text{A22})$$

⁸ Notice that the distribution of the viewing direction should be not $N(\Theta)d\Theta = \sin\Theta d\Theta$ in this scenario, because the viewing direction is related to the trajectory plane of the accelerated particle, see Figure 14.9 and Section 14 in Jackson (1998) for a detailed discussion.

with

$$\dot{\vec{\beta}}_{\tilde{\omega}} \equiv \int_{-\infty}^{\infty} \dot{\vec{\beta}} e^{i\tilde{\omega}t'} dt' \quad \text{and} \quad \tilde{\omega} \equiv (1 - \vec{n} \cdot \vec{\beta})\omega. \quad (\text{A23})$$

where t' is the retarded time. In the ultrarelativistic case, the longitudinal acceleration is smaller than the transverse acceleration, $\dot{\beta}_{\parallel}/\dot{\beta}_{\perp} \sim 1/\gamma^2 \ll 1$. Thus, $\dot{\vec{\beta}}$ and $\vec{\beta}$ are approximately perpendicular to each other, $\dot{\vec{\beta}} \perp \vec{\beta}$. Since both \vec{n} and $\vec{\beta}$ are approximately constant in the above equation, the properties of the spectrum and polarization are mainly determined by the acceleration $\dot{\vec{\beta}}$.

First, we discuss the general properties of the polarization in the scenario with $\gamma\psi \ll 1$. Since both \vec{n} and $\vec{\beta}$ are approximately constant in Eq.(A22), the spectral properties are mainly determined by the acceleration $\dot{\vec{\beta}}$. Choosing a coordinate system S with z -direction pointing toward the observer and with the particle velocity on the $y-z$ plane, thus $\vec{n} = (0, 0, 1)$ and $\vec{\beta} = (0, \sin\theta, \cos\theta)$. In the coordinate system S' with z' -direction pointing toward the particle velocity $\vec{\beta}$ and x' -axis parallel with x -axis, the acceleration could be written as $\dot{\vec{\beta}}' = (b \cos\phi, b \sin\phi, 0)$, where $b = |\dot{\vec{\beta}}'|$ and ϕ is the azimuth angle of $\dot{\vec{\beta}}'$ in the $x'-y'$ plane that is perpendicular to z' -direction. Thus, the acceleration in the S coordinate system is $\dot{\vec{\beta}} = (b \cos\phi, b \sin\phi \cos\theta, -b \sin\phi \sin\theta)$. According to Eq.(A22), the radiation polarization property is determined by

$$\vec{n} \times [(\vec{n} - \vec{\beta}) \times \dot{\vec{\beta}}] = [-b \cos\phi(1 - \cos\theta), b \sin\phi(1 - \cos\theta), 0], \quad (\text{A24})$$

leading to

$$A_{\parallel}(\tilde{\omega}) \propto - \int b(t) \cos\phi(t) e^{i\tilde{\omega}t} dt, \quad (\text{A25})$$

$$A_{\perp}(\tilde{\omega}) \propto \int b(t) \sin\phi(t) e^{i\tilde{\omega}t} dt. \quad (\text{A26})$$

Based on Eq.(A5) and Eq.(A6), we can easily prove that: (1) If the acceleration is always on a straight line perpendicular to $\vec{\beta}$, i.e., $\phi = \text{const.}$, the polarization is fully linear with $\pi_L = 1$; (2) If the acceleration rotates with a constant angular velocity Ω on the plane perpendicular to $\vec{\beta}$, i.e., $\phi(t) = \Omega t$ and $b(t) = \text{const.}$, the polarization is fully circular with $\pi_V = 1$.

In order to obtain the accurate spectrum and polarization, a simpler and more intuitive processing method is to calculate the radiation in the particle comoving frame K' with velocity $\beta_{\parallel} = \beta \cos\psi$ related to the observer frame K , then transfer the radiation to the K frame via Lorentz and Doppler transformations. In the K' frame, the particle moves with the velocity

$$\beta' \simeq \frac{\beta_{\perp}}{\gamma(1 - \beta_{\parallel}^2)} = \frac{(\gamma^2 - 1)^{1/2} \sin\psi}{\cos^2\psi + \gamma^2 \sin^2\psi} \simeq \gamma\psi \ll 1. \quad (\text{A27})$$

Thus, the particle in the K' frame is non-relativistic for $\gamma\psi \ll 1$. In many astrophysical scenarios, the perpendicular acceleration of a charged particle is usually attributed to the Lorentz force by magnetic fields, meanwhile, the intrinsic variation timescale of the magnetic field is longer than Δt_{acc} . In this case, the radiation in the K' frame is cyclotron-like. We consider that in the K' frame the acceleration curvature radius is ρ' , and the angle between the line of sight and the trajectory plane is θ' . We define

$$\zeta \equiv m\beta' \sin\theta' \quad (\text{A28})$$

with m as the harmonic number, then in the K' frame, the radiation power per unit solid angle in the m -th harmonic is (Landau & Lifshitz 1975; Jackson 1998)

$$\frac{dP'_m}{d\Omega} = \frac{e^2 \omega_0^4 m^2}{8\pi^3 c} \left| -\epsilon_{\parallel}' A'_{\parallel}(\omega) + \epsilon_{\perp}' A'_{\perp}(\omega) \right|^2 \quad (\text{A29})$$

with

$$A'_{\parallel}(\omega) = \frac{2\pi i\rho'}{c} \frac{dJ_m(\zeta)}{d\zeta}, \quad (\text{A30})$$

$$A'_{\perp}(\omega) = \frac{2\pi\rho'}{c} \frac{\cot\theta'}{\beta'} J_m(\zeta), \quad (\text{A31})$$

where the fundamental frequency is

$$\omega_0 = \frac{\beta'c}{\rho'}. \quad (\text{A32})$$

In particular, if the gyration motion is caused by the Lorentz force of the magnetic field, one has $\omega_0 = \omega'_B = eB/m_e c$, where ω'_B is the cyclotron frequency in the K' frame. According to Eq.(A5), Eq.(A6), Eq.(A30) and Eq.(A31), the linear polarization degree is

$$\pi_L = \left| \frac{[dJ_m(\zeta)/d\zeta]^2 - (\cot^2\theta'/\beta'^2)J_m^2(\zeta)}{[dJ_m(\zeta)/d\zeta]^2 + (\cot^2\theta'/\beta'^2)J_m^2(\zeta)} \right|, \quad (\text{A33})$$

and the circular polarization degree is

$$\pi_V = \left| \frac{2[dJ_m(\zeta)/d\zeta](\cot\theta'/\beta')J_m(\zeta)}{[dJ_m(\zeta)/d\zeta]^2 + (\cot^2\theta'/\beta'^2)J_m^2(\zeta)} \right|. \quad (\text{A34})$$

Due to $\beta' \ll 1$, the emission but the fundamental frequency $m = 1$ can be neglected, leading to an extremely narrow spectrum. Using the properties of Bessel function $J_m(x) \sim [1/\Gamma(m+1)](x/2)^m$ for $0 < x \ll (m+1)^{1/2}$, the radiation power reduces to

$$\mathcal{P}'_{\omega} \equiv \frac{dP'_m}{d\omega d\Omega} = \frac{e^2\omega_0^2\beta'^2}{8\pi c} (1 + \cos^2\theta') \delta(\omega' - \omega_0). \quad (\text{A35})$$

The linear polarization degree is

$$\pi'_L = \left| \frac{1 - \cos^2\theta'}{1 + \cos^2\theta'} \right|, \quad (\text{A36})$$

and the linear polarization degree is

$$\pi'_V = \left| \frac{2\cos\theta'}{1 + \cos^2\theta'} \right|. \quad (\text{A37})$$

Using the following transformations

$$\cos\theta' = \frac{\cos\theta - \beta_{\parallel}}{1 - \beta_{\parallel}\cos\theta} \simeq \frac{1 - \gamma^2\theta^2}{1 + \gamma^2\theta^2}, \quad (\text{A38})$$

$$\omega' = \omega \frac{1 - \beta_{\parallel}\cos\theta}{(1 - \beta_{\parallel}^2)^{1/2}} \simeq \frac{\omega}{2\gamma} (1 + \gamma^2\theta^2), \quad (\text{A39})$$

$$\mathcal{P}_{\omega} = \mathcal{P}'_{\omega} \frac{(1 - \beta_{\parallel}^2)^{3/2}}{(1 - \beta_{\parallel}\cos\theta)^3} \simeq \mathcal{P}'_{\omega} \frac{8\gamma^3}{(1 + \gamma^2\theta^2)^3}, \quad (\text{A40})$$

the received radiation power is

$$\mathcal{P}_{\omega} = \frac{e^2\gamma^2\psi^2\omega^4}{4\pi c\omega_0^2} \left(1 - \frac{\omega}{\gamma\omega_0} + \frac{\omega^2}{2\gamma^2\omega_0^2} \right) \delta\left(\omega - \frac{2\gamma\omega_0}{1 + \gamma^2\theta^2}\right). \quad (\text{A41})$$

Note that the radiation power \mathcal{P}_{ω} in Eq.(A40) is emphasized to be the received specific power in the K frame, and a factor of $\gamma^3(1 + \beta\cos\theta')^3$ should be corrected from the emitted specific power, see Section 4.8 of Rybicki & Lightman (1986) and involve $d\omega = \gamma(1 + \beta\cos\theta')d\omega'$ to calculate the specific radiation power. We define

$$\bar{\omega} \equiv \frac{\omega}{\gamma\omega_0}, \quad (\text{A42})$$

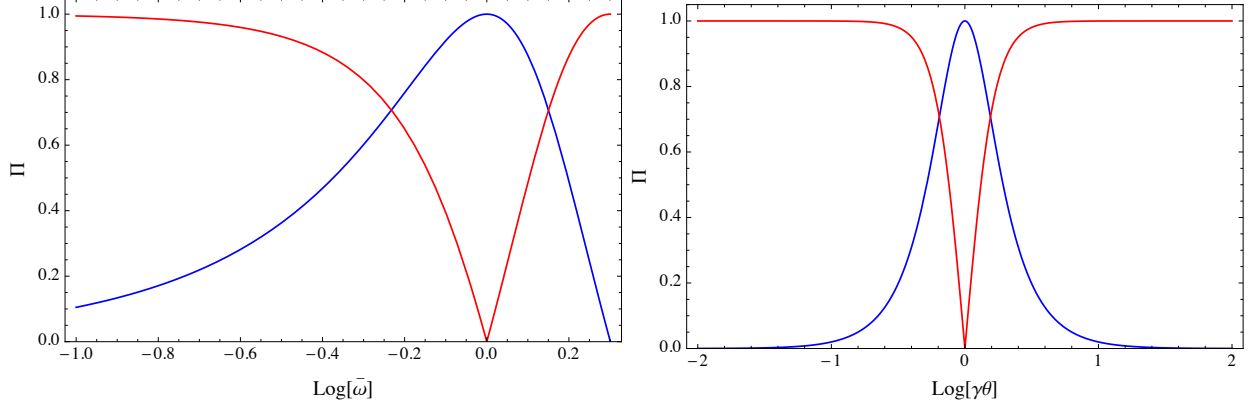


Figure 13. The relations between the polarization degree Π and the dimensionless frequency $\bar{\omega}$ and the viewing angle $\gamma\theta$ for a single radiating particle with $\gamma\psi \ll 1$. The blue and red lines correspond to the linear and circular polarization degrees, respectively. The top panel shows the polarization degree Π as the function of the dimensionless frequency $\bar{\omega}$. The bottom panel shows the polarization degree Π as the function of the viewing angle $\gamma\theta$. The dimensionless frequency $\bar{\omega}$ and the viewing angle $\gamma\theta$ are related via $\bar{\omega} = 2/(1 + \gamma^2\theta^2)$.

then the received radiation power can be rewritten as

$$\mathcal{P}_\omega = \frac{e^2\gamma^5\psi^2\omega_0}{4\pi c}\bar{\omega}^4 \left(1 - \bar{\omega} + \frac{1}{2}\bar{\omega}^2\right) \delta\left(\bar{\omega} - \frac{2}{1 + \gamma^2\theta^2}\right), \quad (\text{A43})$$

and the radiation only occurs at the direction θ with

$$\gamma\theta = \left(\frac{2}{\bar{\omega}} - 1\right)^{1/2}. \quad (\text{A44})$$

Notice that the particle's deflection angle ψ only affects the normalized radiation power but not the typical frequency and the spectral shape. According to Eq.(A43), for a certain viewing direction $\gamma\theta$, the emission is only at the frequency $\bar{\omega} = 2/(1 + \gamma^2\theta^2)$. Thus, the radiation spectrum of a single particle is extremely narrow. Since most radiation energy is emitted with the direction satisfying $\gamma\theta \lesssim 1$, the typical radiation frequency is $\bar{\omega} \sim$ a few (corresponding to $\omega \sim \gamma\omega_0$), which is consistent with the above result estimated by Eq.(15).

Since the polarization degree is Lorentz invariance, according to Eq.(A36), Eq.(A37) and Eq.(A38), the linear and circular polarization degrees are

$$\pi_L = \left|\frac{2\gamma^2\theta^2}{1 + \gamma^4\theta^4}\right| = \left|\frac{2\bar{\omega} - \bar{\omega}^2}{\bar{\omega}^2 - 2\bar{\omega} + 2}\right|, \quad (\text{A45})$$

$$\pi_V = \left|\frac{1 - \gamma^4\theta^4}{1 + \gamma^4\theta^4}\right| = \left|\frac{2\bar{\omega} - 2}{\bar{\omega}^2 - 2\bar{\omega} + 2}\right|. \quad (\text{A46})$$

In particular, $\gamma\theta > 1$ and $\gamma\theta < 1$ correspond to the opposite (left and right) circular polarization, respectively. In Figure 13, we plot the linear and circular polarization degrees Π_i with $i = L$ and V as the functions of the dimensionless frequency $\bar{\omega}$ and viewing angle $\gamma\theta$, respectively. The blue and red lines correspond to the linear and circular polarization degrees, respectively. The top and bottom panels show the polarization degree Π as the functions of the dimensionless frequency $\bar{\omega}$ and the viewing angle $\gamma\theta$, respectively. We can see that high linear polarization (low circular polarization) mainly occur at $\bar{\omega} \sim 1$ and $\gamma\theta \sim 1$, otherwise, low linear polarization (high circular polarization) is dominant.

Furthermore, we consider that multiple radiating particles are uniformly distributed in a three-dimensional beaming with an opening angle Θ_j . The number of the charged particles within $(\Theta, \Theta + d\Theta)$ is

$$N_e(\Theta)d\Theta = N_{e,0} \sin \Theta d\Theta. \quad (\text{A47})$$

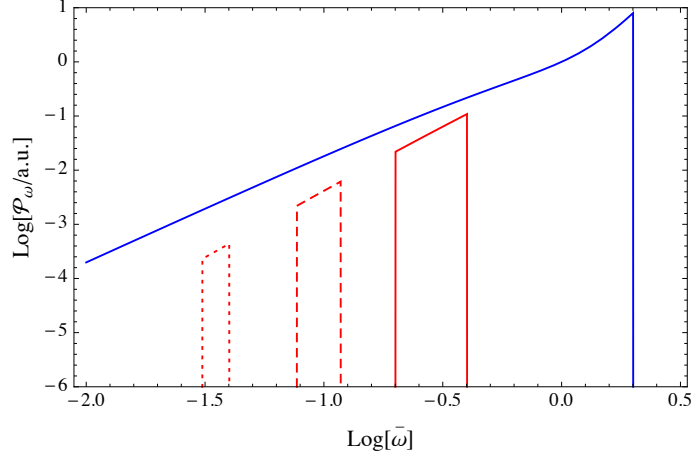


Figure 14. The spectra that are applicable for multiple radiating particles with $\gamma\psi \ll 1$. The blue and red line corresponds to the on-beam case given by Eq.(A48) and the off-beam case given by Eq.(A49), respectively. The red solid, dashed and dotted lines correspond to $\gamma\Theta = 3, 5$ and 8 , respectively. Here $\gamma\Theta_j = 1$ is taken. The unit of \mathcal{P}_ω is arbitrary. For easy comparison with different scenarios, the spectra of the off-beam cases are multiplied by an arbitrary factor in this figure.

When the viewing direction points to the beaming center $\Theta = 0$, the radiation spectrum by multiple particles might be approximately given by

$$\begin{aligned} \mathcal{P}_\omega(\Theta = 0) &\propto \int_0^{\Theta_j} \mathcal{P}_\omega(\gamma\Theta) \sin \Theta d\Theta \\ &\propto \bar{\omega}^4 - 2\bar{\omega}^3 + 2\bar{\omega}^2 \quad \text{for } \bar{\omega}_{\min} = \frac{2}{1 + \gamma^2\Theta_j^2} < \bar{\omega} < 2, \end{aligned} \quad (\text{A48})$$

where $\Theta_j \ll 1$ is assumed in the above equation. Outside the particles' beam $\Theta \gg \Theta_j$, the radiation spectrum by multiple particles might be approximately given by

$$\begin{aligned} \mathcal{P}_\omega(\Theta) &\propto \int_{\Theta - \Theta_j}^{\Theta} \mathcal{P}_\omega(\gamma\Theta) d\Theta \propto \frac{\bar{\omega}^5 - 2\bar{\omega}^4 + 2\bar{\omega}^3}{(2\bar{\omega} - \bar{\omega}^2)^{1/2}} \\ \text{for } \bar{\omega}_{\min} &= \frac{2}{1 + \gamma^2\Theta^2} < \bar{\omega} < \bar{\omega}_{\max} = \frac{2}{1 + \gamma^2(\Theta - \Theta_j)^2}. \end{aligned} \quad (\text{A49})$$

Notice that a factor of $\sin \Theta$ should be involved in the above equation for the viewing direction outside the particles' beam. In Figure 14, we plot the spectra for $\Theta_j = 0$ and $\Theta \gg \Theta_j$ given by Eq.(A48) and Eq.(A49), respectively. For the case of $\Theta_j = 0$, the peak frequency is at $\bar{\omega} \sim 2$ near which the spectrum is narrow due to $\mathcal{P}_\omega \propto \bar{\omega}^4$. For the case of $\Theta \gg \Theta_j$, the spectrum is much narrower, i.e., $\Delta\bar{\omega}/\bar{\omega} \simeq 2\Theta_j/\Theta \ll 1$. Meanwhile, the larger the viewing angle Θ , the narrower the spectrum and the lower the peak radiation power. At last, we should notice that the above discussion assumes that all radiating particles have the same Lorentz factor γ . The distribution of γ for multiple particles would make the spectra relatively wider.

The observed linear and circular polarization degrees depend on the gyration directions of the radiating particles and whether the viewing direction is within Θ_j . If all radiating particles have the same gyration directions, clockwise or anticlockwise, the linear and circular polarization degrees of the multiple particles might be written as

$$\Pi_L \simeq \begin{cases} 0, & \text{for } \Theta \leq \Theta_j, \\ \pi_L(\Theta - \Theta_j), & \text{for } \Theta > \Theta_j, \end{cases} \quad (\text{A50})$$

and

$$\Pi_V \simeq \begin{cases} 1, & \text{for } \Theta \leq \Theta_j, \\ \pi_V(\Theta - \Theta_j), & \text{for } \Theta > \Theta_j, \end{cases} \quad (\text{A51})$$

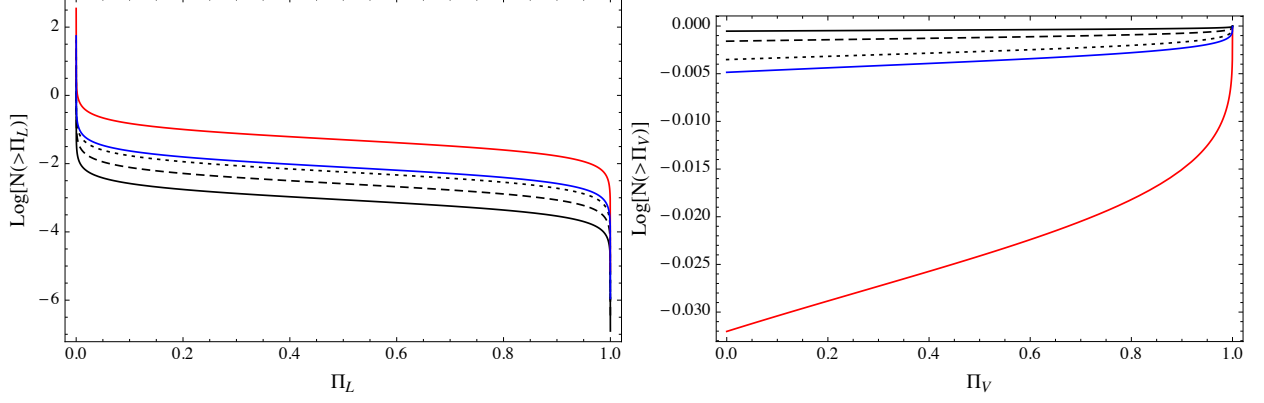


Figure 15. The cumulative distribution of the linear (top panel) and circular (bottom panel) polarization degrees. The distribution function of the viewing direction is assumed to satisfy Eq.(A47). The black solid, dashed and dotted lines correspond to $\gamma\theta_j = 3, 10$ and 30 , respectively for $\gamma\theta_{th} = 100$. The solid red, blue and black lines correspond to $\gamma\theta_{th} = 10, 30$ and 100 , respectively for $\gamma\theta_j = 3$. $\gamma = 100$ is taken here. Different from Figure 12, the y -axis is $\log[N(> \Pi_L)]$ here.

respectively, similar to the discussion in Section 3.1. Notice that different from the above scenario with $\gamma\psi \gg 1$, the on-beam radiation for $\gamma\psi \ll 1$ is dominated by the $\sim 100\%$ circular polarization. On the other hand, if the gyration directions of the particles are random, their polarizations would cancel out. In the following discussion, we are mainly interested in the former scenario.

Since the viewing direction is random in the solid angle, the number of the observable burst within $(\Theta, \Theta + d\Theta)$ is given by

$$N(\Theta)d\Theta = \sin\Theta d\Theta \quad \text{for } 0 \leq \Theta \leq \Theta_j + \theta_{th}, \quad (\text{A52})$$

otherwise, $N(\Theta)d\Theta = 0$, where $\Theta_j + \theta_{th}$ corresponds to the lower limit of the frequency $\bar{\omega}$ or the lower limit of \mathcal{P}_ω . According the polarization properties given by Eq.(A45) and Eq.(A46), the polarization is $\sim 100\%$ circular except $\gamma\theta \sim 1$. Therefore, the cumulative distribution of the linear polarization degrees for multiple radiating particles is

$$N(> \Pi_L) \simeq \frac{\sin\Theta_j \Delta\theta_L}{1 - \cos(\Theta_j + \theta_{th})}, \quad (\text{A53})$$

where $\Delta\theta_L = \theta_{L,2} - \theta_{L,1}$ with $\theta_{L,i}$ solved by Eq.(A45), and $\Delta\theta_L \ll 1$ is used in the above equation.

$$\Delta\theta_L = \frac{1}{\gamma\Pi_L^{1/2}} \left[\left(1 + \sqrt{1 - \Pi_L^2}\right)^{1/2} - \left(1 - \sqrt{1 - \Pi_L^2}\right)^{1/2} \right]. \quad (\text{A54})$$

Similarly, the cumulative distribution of the circular polarization degree is

$$N(> \Pi_V) \simeq 1 - \frac{\sin\Theta_j \Delta\theta_V}{1 - \cos(\Theta_j + \theta_{th})} \quad (\text{A55})$$

where $\Delta\theta_V$ is solved by Eq.(A46), leading to

$$\Delta\theta_V = \frac{2}{\gamma} \left(\frac{1 - \Pi_V}{1 + \Pi_V} \right)^{1/4}. \quad (\text{A56})$$

In Figure 15, we plot the cumulative distribution of the linear (top panel) and circular (bottom panel) polarization degrees, respectively. We can see that for multiple radiating particles, the polarization of this radiation mechanism is almost 100% circular polarization. Thus, if the radiation mechanism of FRBs corresponds to this scenario with $\gamma\psi \ll 1$, the observed moderate number fraction between linearly polarized bursts and circularly polarized bursts of FRB 20201124A (Jiang et al. 2022) might be due to the propagation effects, because the intrinsic polarization of this mechanism is predicted to be $\sim 100\%$ circular polarized. Notice that this result is based on the assumption that all radiating particles have the same gyration direction. If the gyration directions of the particles are random, their polarizations would cancel out.

REFERENCES

- Bannister, K. W., Stevens, J., Tuntsov, A. V., et al. 2016, *Science*, 351, 354
- Barnacka, A., Glicenstein, J. F., & Moderski, R. 2012, *PhRvD*, 86, 043001
- Beloborodov, A. M. 2017, *ApJL*, 843, L26
- . 2020, *ApJ*, 896, 142
- . 2022, *PhRvL*, 128, 255003
- Bhardwaj, M., Gaensler, B. M., Kaspi, V. M., et al. 2021, *ApJL*, 910, L18
- Bochenek, C. D., Ravi, V., Belov, K. V., et al. 2020, *Nature*, 587, 59
- CHIME/FRB Collaboration, Andersen, B. C., Bandura, K. M., et al. 2020, *Nature*, 587, 54
- CHIME/FRB Collaboration, Amiri, M., Andersen, B. C., et al. 2021, *ApJS*, 257, 59
- Clegg, A. W., Fey, A. L., & Lazio, T. J. W. 1998, *ApJ*, 496, 253
- Cooper, A. J., & Wijers, R. A. M. J. 2021, *MNRAS*, 508, L32
- Cordes, J. M., Wasserman, I., Hessels, J. W. T., et al. 2017, *ApJ*, 842, 35
- Dermer, C. D., & Menon, G. 2009, *High Energy Radiation from Black Holes: Gamma Rays, Cosmic Rays, and Neutrinos*, Princeton University Press
- Epstein, R. I. 1973, *ApJ*, 183, 593
- Er, X., Yang, Y.-P., & Rogers, A. 2020, *ApJ*, 889, 158
- Fiedler, R. L., Dennison, B., Johnston, K. J., & Hewish, A. 1987, *Nature*, 326, 675
- Ginzburg, V. L., & Syrovatskii, S. I. 1969, *ARA&A*, 7, 375
- Gould, A. 1992, *ApJL*, 386, L5
- Jackson, J. D. 1998, *Classical Electrodynamics* (3rd Edition, New York: Wiley)
- Jiang, J.-C., Wang, W.-Y., Xu, H., et al. 2022, *Research in Astronomy and Astrophysics*, 22, 124003
- Katz, J. I. 2014, *PhRvD*, 89, 103009
- . 2018, *MNRAS*, 481, 2946
- Kirsten, F., Marcote, B., Nimmo, K., et al. 2022, *Nature*, 602, 585
- Kompaneets, A. S. 1957, *Soviet Journal of Experimental and Theoretical Physics*, 4, 730
- Kremer, K., Piro, A. L., & Li, D. 2021, *ApJL*, 917, L11
- Kumar, P., & Bošnjak, Ž. 2020, *MNRAS*, 494, 2385
- Kumar, P., Gill, R., & Lu, W. 2022, *MNRAS*, 516, 2697
- Kumar, P., Lu, W., & Bhattacharya, M. 2017, *MNRAS*, 468, 2726
- Kumar, P., Shannon, R. M., Flynn, C., et al. 2021, *MNRAS*, 500, 2525
- Landau, L. D., & Lifshitz, E. M. 1975, *The classical theory of fields*
- Law, C. J., Abruzzo, M. W., Bassa, C. G., et al. 2017, *ApJ*, 850, 76
- Li, C. K., Lin, L., Xiong, S. L., et al. 2021, *Nature Astronomy*, 5, 378
- Liu, Z.-N., Wang, W.-Y., Yang, Y.-P., & Dai, Z.-G. 2023, *ApJ*, 943, 47
- Lu, W., Beniamini, P., & Kumar, P. 2022, *MNRAS*, 510, 1867
- Lu, W., Kumar, P., & Zhang, B. 2020, *MNRAS*, 498, 1397
- Lyubarsky, Y. 2014, *MNRAS*, 442, L9
- . 2021, *Universe*, 7, 56
- Lyubarsky, Y., & Ostrovska, S. 2016, *ApJ*, 818, 74
- Mahlmann, J. F., Philippov, A. A., Levinson, A., Spitkovsky, A., & Hakobyan, H. 2022, *ApJL*, 932, L20
- Medvedev, M. V. 2000, *ApJ*, 540, 704
- Melrose, D. B. 1978, *ApJ*, 225, 557
- Mereghetti, S., Savchenko, V., Ferrigno, C., et al. 2020, *ApJL*, 898, L29
- Metzger, B. D., Margalit, B., & Sironi, L. 2019, *MNRAS*, 485, 4091
- Pleunis, Z., Good, D. C., Kaspi, V. M., et al. 2021, *ApJ*, 923, 1
- Qu, Y., Kumar, P., & Zhang, B. 2022, *MNRAS*, 515, 2020
- Qu, Y., & Zhang, B. 2023, *MNRAS*, arXiv:2302.09697
- Qu, Y., Zhang, B., & Kumar, P. 2023, *MNRAS*, 518, 66
- Ridnaia, A., Svinkin, D., Frederiks, D., et al. 2021, *Nature Astronomy*, 5, 372
- Rybicki, G. B., & Lightman, A. P. 1986, *Radiative Processes in Astrophysics* (New York: Wiley-Interscience)
- Sarachik, E. S., & Schappert, G. T. 1970, *PhRvD*, 1, 2738
- Syunyaev, R. A. 1971, *Soviet Ast.*, 15, 190
- Tavani, M., Casentini, C., Ursi, A., et al. 2021, *Nature Astronomy*, 5, 401
- Wang, J.-S., Yang, Y.-P., Wu, X.-F., Dai, Z.-G., & Wang, F.-Y. 2016, *ApJL*, 822, L7
- Wang, W.-Y., Jiang, J.-C., Lee, K., Xu, R., & Zhang, B. 2022a, *MNRAS*, 517, 5080
- Wang, W.-Y., Yang, Y.-P., Niu, C.-H., Xu, R., & Zhang, B. 2022b, *ApJ*, 927, 105
- Waxman, E. 2017, *ApJ*, 842, 34
- Wilson, D. B. 1982, *MNRAS*, 200, 881
- Xu, H., Niu, J. R., Chen, P., et al. 2022, *Nature*, 609, 685
- Xu, S., & Zhang, B. 2017, *ApJ*, 835, 2
- Yang, Y.-P., Lu, W., Feng, Y., Zhang, B., & Li, D. 2022, *ApJL*, 928, L16
- Yang, Y.-P., & Zhang, B. 2018a, *ApJ*, 868, 31
- . 2018b, *ApJL*, 864, L16
- . 2020, *ApJL*, 892, L10
- . 2021, *ApJ*, 919, 89

- . 2023, arXiv e-prints, arXiv:2301.12125
- Yang, Y.-P., Zhu, J.-P., Zhang, B., & Wu, X.-F. 2020, ApJL, 901, L13
- Zhang, B. 2020, ApJL, 890, L24
- . 2022a, ApJ, 925, 53
- . 2022b, arXiv e-prints, arXiv:2212.03972
- Zhang, Y.-K., Li, D., Zhang, B., et al. 2023, arXiv e-prints, arXiv:2304.14665
- Zhou, D. J., Han, J. L., Zhang, B., et al. 2022, Research in Astronomy and Astrophysics, 22, 124001